

Topographic analysis for mapping dunes and assessing dune field resilience using multitemporal LiDAR at White Sands, New Mexico

Brennan W. Young: Texas A&M University (brennan1young@gmail.com)

Don R. Hood: Baylor University

Michael P. Bishop: Texas A&M University

Ryan C. Ewing: Texas A&M University

David Bustos: U.S. National Park Service

This manuscript was submitted for publication in *Aeolian Research*. Please note that the manuscript was rejected during its third peer review cycle. The authors understand the principal reasons for rejection to be the article's length and a desire for significant additional research to quantify spatial and semantic uncertainty in the context of the landform boundaries. Please feel free to contact the corresponding author to provide feedback or discuss the manuscript.

Topographic analysis for mapping dunes and assessing dune field resilience using multitemporal LiDAR at White Sands, New Mexico

Brennan W. Young^{1*}, Don R. Hood², Michael P. Bishop³, Ryan C. Ewing¹, David Bustos⁴

¹Texas A&M University, Department of Geology & Geophysics, College Station, Texas, USA.

²Baylor University, Department of Geosciences, Waco, Texas, USA.

³Texas A&M University, Department of Geography, College Station, Texas, USA.

¹Texas A&M University, Department of Geology & Geophysics, College Station, Texas, USA.

⁴National Park Service, White Sands National Park, Holloman AFB, New Mexico, USA.

*Corresponding author Brennan W. Young. brennan1young@gmail.com

Abstract

Sand dune morphology is indicative of complex system interactions at a wide range of spatial and temporal scales that govern dune topographic structure. We created an object-oriented topographic framework based on slope attitude, curvature, and contextual analysis to map and characterize sand dune morphology at White Sands National Park, New Mexico, USA that limits empiricism and reliance on *a priori* knowledge of dune field structure and dynamics. We used eight LiDAR-derived digital elevation models with our framework to segment sand dunes and characterize dune morphology from 2007 to 2020 and evaluated dune field behavior and resilience. The segmentation is 92% accurate relative to manual mapping. From the segmentation, we calculated dune statistics, including height, width, length, area, volume, area-surface area ratio, circularity, migration rate, and aggradation rate. We found these statistics compared well with prior research. We identified a trend toward fewer dunes with greater area and volume from 2007 to 2020, which may be related to typical dune field maturation or short-term (seasonal to decadal) fluctuations related to weather and dune processes. Changes in dune migration rate and sand flux depended on the strength and directionality of seasonal southwesterly winds and likely periods of intense precipitation or drought. Trends identified in this study can be considered a baseline from which longterm trends identified through on-going monitoring can be evaluated. This research highlights current dependence on incomplete models for mapping and characterizing dunes and landscape resilience, and the need to quantitatively formalize numerous geomorphological concepts.

key words: White Sands, LiDAR, geomorphology, geomorphometry, spatial structure, resilience

1 Introduction

Aeolian dune field spatial patterns are governed by multiscale and multitemporal sand-fluid, fluid-dune, and dune-dune interactions operating within geologic and climate boundary conditions (Bagnold, 1941; Lancaster, 1995; Werner, 1999; Werner and Kocurek, 1999; Claudin and Andreotti, 2006; Ewing and Kocurek, 2010; Ewing et al., 2015; Kocurek and Ewing, 2016; Grohmann et al., 2020). These interactions give rise to dune-field patterns, which have numerous measurable parameters related to the processes that govern dune morphology and spatial distribution (Claudin and Andreotti, 2006; Kocurek et al., 2007; Baitis et al., 2014; Day and Kocurek, 2018; Duran Vinent et al., 2019; Gadal et al., 2020). Consequently, mapping dunes and measuring aspects of dune morphology from that mapping yields insight into the long-term behavior of the aeolian system and the resilience of the system to climatic or other external forcing factors and boundary conditions (Ewing et al., 2006, 2015; Rachal and Dugas, 2009; Ewing and Kocurek, 2010; Houser et al., 2015). Typically, mapping the spatial structure of dune fields is done using optical aerial or satellite images (Breed and Grow, 1979; Ewing et al., 2006; Day and Kocurek, 2018). High spatial resolution, wide spatial coverage, accessibility, and ease of use in a GIS environment make optical images efficient to use for mapping, however many of the parameters recognized as important for dune-field pattern analysis (Ewing et al., 2006), including crestlines and dune boundaries (e.g., defects) are inferred based on the mappers interpretation of the images against a prototypical model of dune topographic structure (e.g., well defined slopes and crest as in a textbook). Many of the elements that cannot be directly determined in 2D images can be measured using 3D dune topography.

Topographic data are increasingly available for Earth and other planetary dune fields and have only recently begun to be used in dune-field scale analysis (Jerolmack et al., 2012; Pedersen et al., 2015; Swanson et al., 2016; Lee et al., 2019; Phillips et al., 2019; Gadal et al., 2020; Rubanenko et al., 2021). Typical approaches to using digital elevation models (DEMs) include area or field-scale statistics (e.g., height, volume) from DEM analysis that show how their statistical distribution (Reitz et al., 2010; Lee et al., 2019) or mapping of individual dunes to extract dune statistics that are similar to the 2D prototypical models (e.g., Baitis et al., 2014; Pedersen et al., 2015; Rubanenko et al., 2021). The former approach is efficient for evaluating entire dune fields, but lacks direct dune-to-dune comparisons important for analyzing dune patterns and dune evolution. Mapping individual dunes with DEMs has been accomplished through manual digitization or through empirical models (Ewing and Kocurek, 2010; Baitis et al., 2014; Pedersen et al., 2015). Manual mapping is problematic because it is time-consuming in the face of an ever-growing volume of data and need for monitoring capabilities, subject to the mappers' biases which may not be replicable, and reliant on a two-dimensional perspective to characterize three-dimensional features (Baitis et al., 2014; Wernette et al., 2018a). Empirical and machine-learning approaches (e.g., Cisneros et al., 2020; Emran et al., 2020; Grohmann et al., 2020; Rubanenko et al., 2021), alleviate issues associated with big-data, but require significant parameter-tuning, assumptions regarding dune structure homogeneity, or *a-priori* knowledge of the geomorphic system. Recent advances in geomorphological mapping use object-oriented approaches to map and evaluate topographic structure (Heckmann et al., 2015; Alvioli et al., 2020; Emran et al., 2020; Young and Bishop, 2022). This approach exploits the 3D nature of DEMs to provide a computational framework for representing spatial scale and topology, and provides field-scale analyses with outputs comparable to prototypical landscape models.

This study used a spatial topographic framework to evaluate dune field topographic structure with the goal to map and characterize sand dune field patterns in three dimensions. This effort explicitly couples concepts from the discipline of geomorphometry, which emphasizes mathematical analysis of landform topography, with aeolian geomorphology. That is, we aimed to formalized landform concepts that can produce measurable results comparable with past studies. We demonstrate our approach with multitemporal, LiDAR-derived DEMs for the dune field at White Sands National Park, New Mexico, USA. We interpret the model results to assess spatiotemporal behavior and resilience of the White Sands Dune Field. Resilience is a multi-faceted topic in geomorphological research, and gaining insight into the long-term behavior of the White Sands aeolian system motivates this research. For the purposes of this research, we understood resilience to broadly mean a tendency to remain or quickly return to some initial or nominal state (Downes et al., 2013; Stallins and Corenblit, 2018; Thoms et al., 2018). We consequently searched for evidence for resilience, or the lack thereof, as significant and persistent changes in dune field morphological parameters or process rates (e.g., dune height, migration rate) in relation to significant weather or climatic events. We

also placed our results in context with prior research on the long-term behavior of the White Sands aeolian system.

2 Background: Geomorphometry and Geomorphological Mapping

Geomorphological mapping has long been a fundamental component of geomorphological research, as Earth scientists attempt to improve our understandings of forcing factors, process regimes, landform evolution, morphodynamics, landscape evolution, and geomorphological systems and resilience (Bishop et al., 2012; Wohl et al., 2014; Bishop and Houser, 2016; Thoms et al., 2018). The literature documents the rapid evolution and use of geospatial technologies to facilitate improved mapping capabilities related to new sensors and data, spatial analysis and modeling approaches, and pattern recognition solutions including artificial intelligence (AI) techniques (Dao et al., 2020; Rubanenko et al., 2021). Nevertheless, mapping remains highly empirical in nature, and there are a multitude of complex and multi-faceted issues that have not been adequately addressed to ensure mapping accuracy and repeatability (Dramis et al., 2011; Bishop et al., 2012; Wheaton et al., 2015; Bishop and Houser, 2016; Thorsnes et al., 2018; Wernette et al., 2018a; Bishop et al., 2020).

Fundamentally, mapping capabilities have significantly improved because of the availability of high-resolution topographic data, new land-surface parameters for characterizing topographic properties (Bishop and Houser, 2016), the use of object-oriented analysis (Minár and Evans, 2008; Eisank, 2010; Eisank et al., 2011; Vaz et al., 2015; Alvioli et al., 2020; Anders et al., 2020; Zhang et al., 2020), and new neural-computing approaches (i.e., deep learning) for identifying complex and non-linear landscape patterns (Dao et al., 2020; Hoese and Kuenzer, 2020; Xie et al., 2020; Rubanenko et al., 2021). Object-oriented analysis aims to segment the land surface into distinct objects, often based on the concepts of homogeneity or landform prototypicality, and has the advantages of (1) producing a map of distinct and geographically meaningful units, providing a basic mapping capability, and (2) spatially representing spatial variation in the sizes and shapes of each spatial unit (Bishop et al., 2020). Machine-learning and deep-learning approaches are effective for pattern-matching capabilities (i.e., to map spatial units based on similar units upon which the models were trained). Most approaches to mapping dune-forms rely upon processing two-dimensional imagery (e.g., Vaz et al., 2015; Rubanenko et al., 2021) which perform well where there is sufficient contrast between the dune and the interdune area. Dune morphometry, however, has yet to be formalized in a way that is conducive for mapping applications. Considerable progress remains to be made in geospatial data science and numerical terrain analysis (i.e., geomorphometry). Outstanding issues in these fields include: (1) landform semantics (Deng, 2007; Eisank et al., 2011; Bishop et al., 2012, 2020); (2) scale, structure, and organization (Lastochkin et al., 2018); (3) indeterminate boundaries (Burrough and Frank, 1996; Fisher et al., 2005; Bishop et al., 2012); (4) error and uncertainty (Bond et al., 2007; Bond, 2015; Brierley et al., 2021); and (5) use of knowledge and analytical reasoning (Bishop et al., 2012; Lastochkin et al., 2018; Brierley et al., 2021; Bishop et al., 2020). Our effort to map White Sands using our geomorphometric approach is motivated by a need to better formalize and digitally represent former advances in characterizing topographic properties and landform structure, and to be able to assess landscape morphodynamics to understand how dunes and dune fields dynamically transition and change over time and characterize their resilience to climate and anthropogenic change (Bishop et al., 2012; Lastochkin et al., 2018; Stallins and Corenblit, 2018; Thoms et al., 2018; Bishop et al., 2020; Young and Bishop, 2022).

3 Study Area

We examined 40 km⁻² of White Sands Dune Field located within White Sands National Park in southern New Mexico (Fig. 1). The dune field sits within the Tularosa Basin and is flanked to the west by the San Andres Mountains and to the east by the Sacramento Mountains. The White Sands Dune Field is a wet aeolian system with a shallow water table (≤ 1.5 m) that recharges from local precipitation and regional aquifers and primarily discharges by evaporation (Newton and Allen, 2014; Newton and Land, 2016). Surface and groundwater flows enriched in sulfur and calcium due to interactions with the surrounding and underlying Paleozoic carbonate and evaporite sequences evaporate in the semi-enclosed basin to give rise to extensive gypsum playa lakes that lie west of the dune field (Ewing, 2020). Lake Otero, the most recent extensive playa lake, existed during the late Pleistocene and created meters of gypsiferous sediments that were subsequently

deflated during the Holocene drying of the southwest USA (Langford, 2003; Allen et al., 2009; Szyrkiewicz et al., 2010; Baitis et al., 2014). Deflation of Lake Otereo sediment gave rise to the modern day dune field, which covers nearly 500 km² across the basin (Baitis et al., 2014). Modern sediment input into the dune field arises from evaporite production in Lake Lucero, the largest modern active playa in the basin, and other ephemerally active playas. Springtime southwesterly winds mobilize sediment from these playas into the dune field. The dominant southwesterly winds and to a lesser extent northerly and southerly winds shape the overall dune-field structure (Pedersen et al., 2015).

Sparsely distributed dome dunes exist in Alkali Flat and give way to sandsheets and protodunes that compose a 700 m wide sand ramp on the western flank of the dune field (McKee, 1966; Phillips et al., 2019). Sediment transport-limited barchanoid ridges transverse to the southwesterly winds emerge from the sand ramp and give way downwind to sediment availability-limited barchan dunes surrounded by extensive interdune flats. The barchan dunes transition into vegetated parabolic dunes before the dune field abruptly terminates 13 km downwind from the upwind sand ramp (Reitz et al., 2010; Pelletier and Jerolmack, 2014).

Dune-field mapping with the goal of evaluating dune and dune field pattern metrics has been conducted at White Sands using optical aerial and satellite data and DEMs (Ewing et al., 2006; Rachal and Dugas, 2009; Baitis et al., 2014; Pedersen et al., 2015; Swanson et al., 2016). Topography at White Sands is spatially heterogeneous, even among the visually regular patterns of transverse and barchanoid dunes (McKee, 1966; Baitis et al., 2014). Dune crest-to-crest wavelength varies between 100 and 250 m with dunes that are typically between 5 and 15 m in height, about 80 m in length from stoss to lee, and wildly variable width and volume but averaging around 450 m in width and 120,000 m³ (Langford, 2003; Rachal and Dugas, 2009; Baitis et al., 2014; Phillips et al., 2019). White Sands dune migration rate is strongly location- and time-dependent, varying between 1 and 6 m yr⁻¹ with sand flux 5–10 m² yr⁻¹ (0.5–1 g m⁻¹ s⁻¹; Watkins et al., 1972; Kocurek et al., 2007; Pedersen et al., 2015; Swanson et al., 2016; Phillips et al., 2019; Gadal et al., 2020; Gunn et al., 2020). This study expands on this prior work by extracting dune topographic data from eight DEMs spanning 2007–2020 at White Sands to establish decadal-scale variability in established pattern parameters, dune morphometry, and dune dynamics.

4 Methods

Our characterization is based upon object-oriented analysis of DEMs. The general steps in this process are: (1) data acquisition; (2) DEM pre-processing; (3) parameterization of the land-surface; (4) partitioning the topography into fundamental terrain units; (5) distinguishing between dune and interdune areas; (6) disaggregation of dune areas into isolated "dune parts;" (7) aggregation of dune parts into dune units; (8) dune-unit post-processing; (9) characterization of dune morphology; (10) characterization of dune dynamics; and (11) comparison to meteorological data to assess of dune field resilience (Fig. 2). Pre-processing, post-processing, dune-dynamics characterization, and data visualization were accomplished with ESRI ArcGIS Pro and Microsoft Excel software; we calculated drift potential with python code; all other processing was accomplished with C++ code.

We use an object-oriented method for abstracting the land surface into distinct spatial units with inherent geometric and geomorphic meaning ((e.g., similar to elementary forms; Minár and Evans, 2008; MacMillan and Shary, 2009; Minár et al., 2020). Because these spatial units are derived from characteristics of the topography, we call them "terrain units." It is through the spatial relationships inherent in the topological network of terrain units that we infer the entire form of distinct dunes. We recognize dunes as fundamentally small-scale "eminences," which are features recognized and defined by their positive relief (Gaurav and Mark, 2010; Young and Bishop, 2022).

4.1 Data and Pre-processing

Dune mapping and characterization was accomplished by analyzing gridded DEMs at 1 m resolution that were derived from airborne LiDAR collected in June 2007, June 2008, January 2009, September 2009, June 2010, August 2015, December 2018, and January 2020 (Table 1). These data have been collected as part of a long-term dune monitoring campaign supported from various sources and are published online at OpenTopography.org and the Texas Data Repository. We suppressed high-frequency DEM error by applying a 3 × 3 mean filter to each dataset.

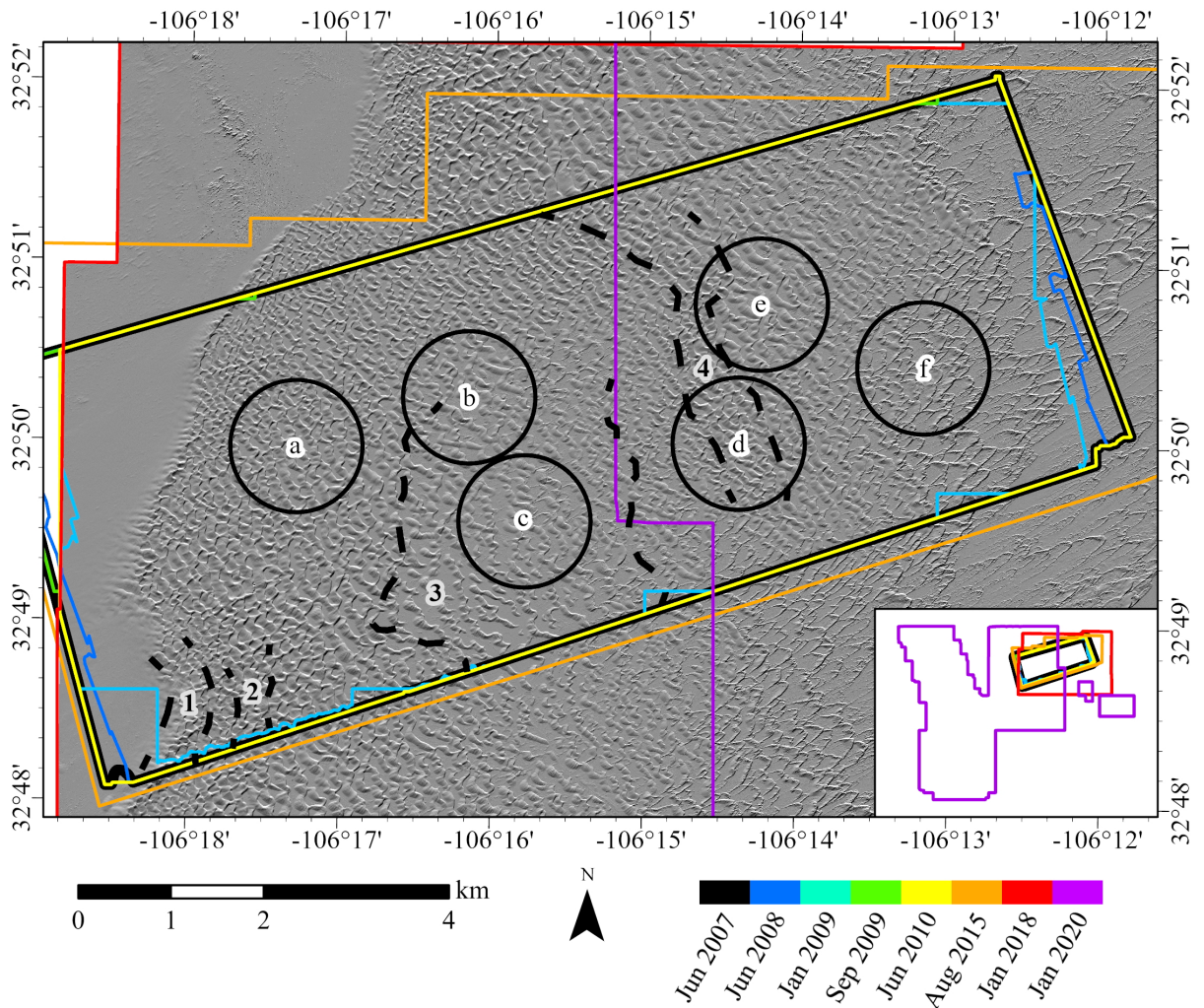


Figure 1: Hillshaded topography of the White Sands dune field. The extents of LiDAR coverage are indicated with colored lines (full extent shown in the inset). Circular Zones selected for parameter evaluation are shown and labeled a–f. Zones a, b, and e were selected to evaluate general west-east changes where dunes are barchanoid and spatially dense, c and d were selected to evaluate areas of relatively sparse barchanoid dunes, and zone f was selected to evaluate parabolic dunes. All zones have a diameter of 1360 m. The edges of the zones studied by Baitis et al. (2014) (1–4) are shown in dashed lines for comparison.

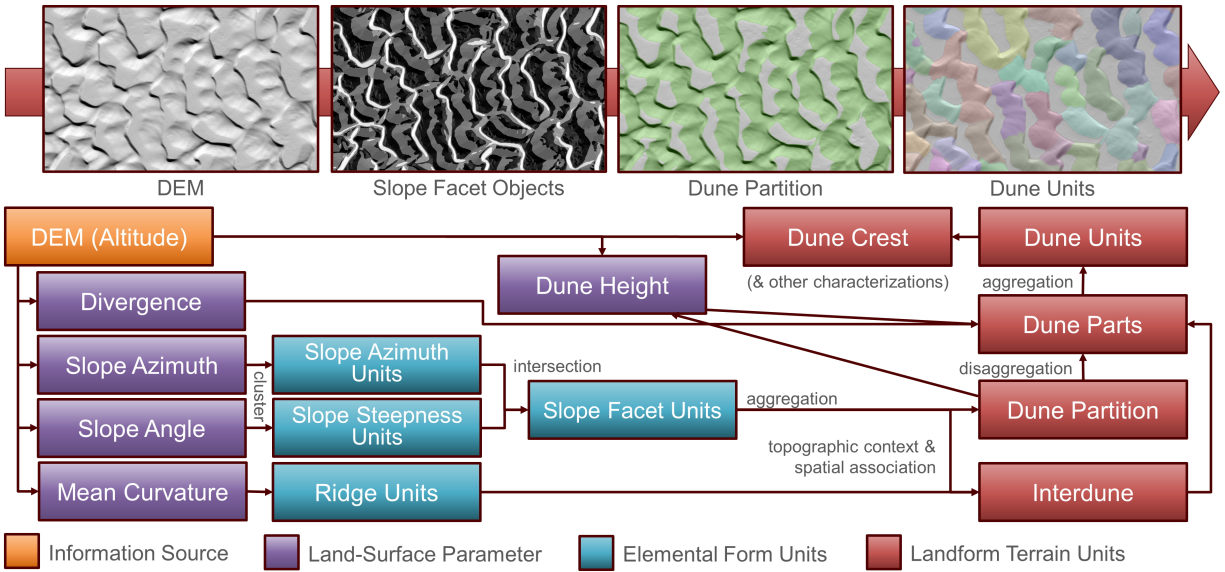


Figure 2: Simplified topographic structural framework, showing the general workflow for mapping dune units.

Table 1: LiDAR datasets used in this study. The dates show the span of time reported for the survey. If the survey spanned multiple days, we used the first date of the survey for our temporal analyses, listed under "Days." Horizontal and vertical accuracy ("Horiz. Acc." and "Vert. Acc.," respectively) are reported in cm; a "-" indicates that accuracy was not reported with the LiDAR survey data. Note that the 2015, 2018, and 2020 datasets are part of the USGS 3DEP program, and the reported accuracy is the RMSE of the 3DEP program overall; otherwise accuracy values are 1 sigma as indicated in the survey report.

Data Collection Dates	Days	Horiz. Acc.	Vert. Acc.	Reference
1 June 2007	0	-	-	Kocurek and Ewing (2020a)
1 June 2008	366	-	-	Kocurek and Ewing (2020b)
24 Jan 2009	603	17 cm	5–35 cm	Kocurek (2013a)
26 Sep 2009	846	17 cm	2–20 cm	Kocurek (2013b)
6 Jun 2010	1101	17 cm	5–35 cm	Ewing (2012)
8–9 Aug 2015	2990	82 cm	53 cm	USGS (2017)
10 Dec 2018–29 Apr 2019	4210	82 cm	53 cm	USGS (2020)
18–19 Jan 2020	4614	82 cm	53 cm	USGS (2021)

Table 2: Land-surface parameters used to map and characterize dune topographic structure.

Parameter	Symbol	Source	Description
Altitude	z	DEM	Surface height, to derive other parameters.
Slope angle	θ	Shary et al. (2002)*	Slope steepness, to discriminate between lee slopes, stoss slopes, and horizontal slopes.
Slope azimuth	φ	Shary et al. (2002)*	Slope facing direction, to distinguish between portions of the dune slope based on facing direction.
Mean curvature	K	Olaya (2009)*	General convexity or "ridge-ness", to distinguish between dune-forms and the interdune area. Mean curvature is computed at three different scales for assessment of multi-scale convexity: 7×7 as with other parameters, 13×13 , and 25×25 .
Slope-azimuth divergence index	SADI	Bishop et al. (2020)	Characterizes the degree to which local topography slopes away from a location. High SADI is characteristic of ridge-like features, such as dune crests, and low SADI is characteristic of convergent areas, including some dune boundaries.

*Altitude gradients computed as per Wood (1996).

Due to computational memory limitations, each DEM was divided east-to-west into four sub-scenes. To limit edge-effects that affect mapping accuracy and to ensure that complete dunes are mapped continuously throughout the study area, each sub-scene overlapped adjacent sub-scenes in excess of two dune wavelengths (about 400 m).

4.2 Land-surface Parameters

We represent fundamental topographic properties as land-surface parameters. Land-surface parameters were computed with a 7×7 window to remove high-frequency noise and small-scale structures that are irrelevant to mapping dunes (i.e., we use a 7×7 -pixel kernel, which averages over a 7×7 m area in our datasets, each of which have 1 m spatial resolution). Altitude gradients needed for parameter calculation are computed by approximating a quadratic surface via linear least squares regression (Wood, 1996).

The land-surface parameters that we computed are slope angle (θ), slope azimuth (φ), mean curvature (K), and the slope-azimuth divergence index (SADI), which are each described in Table 2.

4.3 Terrain Units

We used an object-oriented approach for abstracting the land surface into structurally significant, approximately homogeneous spatial units that adapt well to the natural scale of topographic variation. The use of terrain units permits us to address spatial context and association that are otherwise challenging to represent computationally. We use the term "unit" to refer to a set of labeled grid cells to which we ascribe meaning. For example, a "slope-facet unit" is a set of grid cells with relatively homogeneous slope aspect and steepness, and each unit has a unique ID. The boundary of a terrain unit is the perimeter that surrounds the set of grid cells belonging to the terrain unit, and any characterization of the boundary may include grid cells on either side of that perimeter line. Using terrain units allows us to abstract the land surface into geometrically significant groups that relate with adjacent units to provide spatial context for our analysis.

The terrain units that we generated are slope-steepness units (SS), slope-azimuth units (SA), slope-facet units (SF), ridge units (R), dune-part units, and dune units. Terrain units and their derivation are described in Table 3.

ISODATA clustering for mapping SS and SA was performed on each sub-dataset so computation could proceed and mapping achieved while isolated to the local dataset being mapped. Because clustering occurs

Table 3: Terrain units used to map dunes.

Terrain Unit	Symbol	Description
Slope-azimuth unit	SA	Areas of homogeneous slope aspect. We divided the terrain into 8 classes of SA using ISODATA in the parameter space defined by $\cos \varphi$ and $\sin \varphi$, as per Young and Bishop (2022).
Slope-steepness unit	SS	Areas of homogeneous slope steepness. We divided the terrain into 3 classes of SS using ISODATA in the parameter space defined by θ . The SS classes represent the general division of slopes in aeolian environments: the flat interdune and dune tops, moderate stoss slopes, and steep lee slopes.
Slope-facet unit	SF	Areas of homogeneous slope attitude, obtained by the spatial intersection of SA and SS.
Ridge unit	R	Concave features of positive mean curvature ($K > 0$) at every scale at which curvature was computed, after Young and Bishop (2022).
Dune-part unit	-	Micro-eminences divided from a dune-interdune partition, local dune height and topographic divergence.
Dune unit	-	Eminences that broadly represent distinct dunes. Dune units were aggregated from dune-part units.

independently in overlapping sub-datasets, SS and SA differ subtly in the overlapping regions, which results in subtly different mapping results in the overlapping areas for each time period. Because slope angle and the sine and cosine of slope azimuth already have constrained ranges, we treated them as already normalized. We observed negligible difference in SS clustering when transforming slope angle by sine or cosine.

4.3.1 Dune-Interdune Partition

Dunes are essentially small-scale topographic eminences (Gaurav and Mark, 2010) and we map them using a method similar to Young and Bishop (2022). We identified eminence-likely areas, and grew those based on spatial context represented principally by SF-unit spatial topology.

Recognizing that any significantly sloping area was not part of the interdune plane, all SF units derived from any but the shallowest SS class were marked as 'dune.' For each 'non-dune' SF unit adjacent to a 'dune' SF unit, we used bilinear interpolation to approximate the substrate from other SF units that met the criteria: (1) the unit's centroid was within 150 m of the centroid of the SF unit being evaluated; (2) the unit was not marked as 'dune; (3) the unit had a lower mean altitude than the SF being evaluated; and (4) the unit exhibited less than 40% overlap with R units. If the altitude of the SF unit exceeded two standard deviations above the height of the approximated surface, then the SF was marked as 'dune.' We iteratively repeated this process until no new SF units were marked as 'dune.' The criteria used to select SF units for the interpolation were based on empirical assessment of the spatial structure to achieve a subjectively distinct divide between dunes and the interdune area: a sufficiently large area needed to be searched for what could possibly be the interdune plane that allowed for morphological complexity within that plane.

We cleaned the dune-interdune partition by identifying small, compact areas that did not match their surroundings (e.g., small 'non-dune' areas completely surrounded by 'dune'). We represented compactness with the circularity ratio (C ; Wilson et al., 2012), and its shape by approximating the radius of the object as if it were an idealized circle:

$$r_o = P^3 / (8\pi^2 A), \quad (1)$$

where P is the unit's perimeter and A is its area. If $r_o < 20$ m and $C > 0.5$, the unit was reclassified to match its neighbors.

4.3.2 Dune Disaggregation

The 'dune' partition was divided into distinct dune objects by identifying more basic dune-part units, evaluating their adjacency structure, and aggregating dune-part units where their boundaries were least characteristic of sand-dune boundaries. We characterized dune boundaries based on dune narrowing with respect to dune height, surface morphology, and planimetric width.

The characterization of dune height depends on an approximation of the topographic surface beneath the dune, which we refer to as the 'dune substrate.' For all areas identified as 'dune,' we used bilinear interpolation to predict the altitude of the dune substrate. Altitude samples were collected radially in 5° increments, up to the first 20 m of the first 'non-dune' area encountered by each ray. Dune height, h , was computed for every grid cell within the 'dune' area as the difference between surface and substrate altitudes (minimum 0).

In order to identify dune-unit boundaries at locations of low dune height and convergent surface morphology, we computed a local dune-volume-morphology index as:

$$v = \max \left(0, \sqrt{\left(\left(\frac{h - h_{\min}}{h_{\max} - h_{\min}} \right)^2 + SADI^2 \right)} \right), \quad (2)$$

where h_{\min} and h_{\max} are the minimum and maximum h for that 'dune' patch.

Dune forms are low-frequency abstractions of the smaller-scale hummocks and mounds bound by locations of relatively low volume or topographic divergence. We mapped these smaller-scale features by identifying local maxima in v and labeling the area that traces up to those maxima on the path of steepest ascent on the v surface. These small-scale units, however, were more representative of small bedforms that do not well represent the hummocks and mounds that together constitute a dune form. A lower-frequency solution was required, which also captured the small-scale nuance of these v -unit boundaries. We generated a new, low-frequency surface such that v^* is the mean v within a 21×21 window restricted to the same 'dune' patch in the dune-interdune partition. By tracing from v -maxima to v^* -maxima on the v^* surface, we relabeled v -units to their common v^* -units, or 'dune parts.' In this way, a low-frequency topographic mound related to dune structure was identified with the shape of its boundary imparted by the high-frequency v . The boundaries between dune-part units were thus lines of low volume and high convergence, which could be assessed to determine whether the boundary separated two dunes, or if the dune parts were components of the same dune.

Because of scale-differences due to the generalization in v^* , some paths to v -maxima cross areas belonging to different v^* -maxima. This was corrected iteratively such that, after the previous labeling step, the path of steepest ascent was again traced from each v -maxima on the v^* surface until a different label was encountered. That label was applied to the area associated with that v -maxima. Small dune-part units at the edges of 'dune' areas were not representative of a significant portion of a dune's volume, specifically when their v^* -maximum was located at the edge of the unit. This was most common at the up-wind edge of the dune field. These dune-part units were aggregated with the adjacent dune-part unit with which its boundary was least 'divisive.' Boundary-divisiveness was defined based on the idea that boundaries exist between adjacent dunes, or dune-pattern defects occur, where the sand body narrows in planimetric width, narrows in height, and exhibits high topographic convergence. We drew an idealized cross-section at the interface between each pair of dune-part units, where that idealized cross-section was parabolic in shape and of a width and height that we linearly interpolated from the adjacent dune-part units. The predicted maximum v of that idealized boundary was:

$$v_{AB} = v_A + d_A \frac{|v_A - v_B|}{d_A + d_B}, \quad (3)$$

where v_A and v_B are the respective maxima in v in dune-part units A and B, and d_A and d_B are the respective distances from the peak- v location in units A and B to the peak- v location on the boundary. The predicted width of the idealized boundary was, assuming circular approximations of dune-part footprints:

$$w_{AB} = \frac{P_A}{\pi} + d_A \frac{|(P_A - P_B)/\pi|}{d_A + d_B}, \quad (4)$$

where P_A and P_B are the respective perimeters of units A and B.

The predicted cross-sectional area of the idealized boundary was:

$$A_{xp} = \frac{2}{3}v_{AB}w_{AB}, \quad (5)$$

and the actual area (A_x) was half the sum of all v for all grid cells adjacent to the boundary multiplied by the resolution of the grid. We characterized boundary divisiveness as:

$$\gamma = \max(0, 1 - \frac{A_x}{A_{xp}}). \quad (6)$$

Dune units were obtained by aggregating dune-part units based on this characterization of their boundaries and their adjacency structure. Because it can be unclear how to merge clustered groups of dune-part units, we simplified the dune-part adjacency structure by not counting dune-part units as adjacent if they exist in a cluster (i.e., they share dune-part neighbors) and have the most divisive boundary in that cluster. We established dune-unit boundaries by retaining dune-part unit boundaries that: (1) did not orphan dune-part units adjacent to only one other dune-part with $\gamma < 0.1$ between them; (2) met an empirically-determined divisiveness threshold of $\gamma > 0.6$; and (3) divided interacting dunes by removing only the least two divisive boundaries between adjacent dune-part units with at least three adjacent dune-part units.

4.4 Post-Processing and Validation

DEMs of White Sands National Park were divided into areas of about 12 km² to reduce computational burden, with about 400 m overlap between DEM sections. The statistical distribution of altitude, slope angle, and slope azimuth were different in each sub-scene, resulting in subtly different aggregated dunes in overlapping areas. Differences between sections are more significant when DEM sections included large areas outside of the dune field. The 400 m overlap ensured that at least one uninterrupted solution was obtained for each dune unit. We applied three guiding principles to manually resolve multiple solutions in overlapping areas:

- **Congruency.** The final dune map should have no gaps except in the interdunes, and dune units should not overlap. Therefore, the borders of each dune unit must be congruent with one another. Where boundaries are incongruent, the dune unit with an incongruent boundary must be removed, though removal of incongruent units often cascaded into other removals due to further incongruency.
- **Parsimony.** We prefer to describe dunes with as few distinct dune units as possible. Therefore, when two solutions describe the same section with a different number of dune units, we favor the solution with fewer dune units.
- **Conceptual affinity.** Where the two datasets describe the same area with the same number of dune units, but with differing boundaries, we selected the dune units that we interpreted to better reflect distinct dunes. We note that small differences can lead to minor incongruencies along boundaries which do not substantially affect the dune statistics.

Where dune units were identical or near-identical, we preserved those originating from the westernmost dataset. We removed dune units that intersected the edges sub-dataset, as they were inherently incomplete and lacking the spatial structural information needed for their construction.

For validation purposes, we manually mapped sand dunes in zones chosen to evaluate dune parameters at a level detail between the individual dune and the entire dataset (Fig. 1). This mapping was conducted by the authors for the June 2008 dataset using a hillshaded DEM at 1:10000 scale. Because manual mapping is a subjective exercise that cannot be exactly replicated by another person, and because drawing boundaries between interacting dunes is highly imprecise, manual mapping focused solely on mapping the area covered with dunes to separate the dune and interdune areas rather than mapping distinct dune boundaries. This provided a baseline against which we compared our automated mapping.

Table 4: Dune unit characteristics.

Characteristic	Symbol	Description
Maximum height	h_{\max}	Peak difference between the surface altitude and the predicted substrate altitude within the dune unit’s area.
Mean height	\bar{h}	Mean difference between the surface altitude and the predicted substrate altitude within the dune unit’s area.
Perimeter	P	Length of dune unit boundary.
Area	A	Planimetric area of dune unit footprint.
Volume	V	$V = \sum h dx^2$, where dx is the grid resolution.
Circularity ratio	C	The spatial compactness of the dune unit’s planimetric area (Wilson et al., 2012).
Surface area	A_s	Computed via Jenness (2004).
Width	W	The length of the dune’s width-line.
Length	L	The average length of the dune perpendicular to the width-line, which we measured as a rectangular approximation: A/W .
Orientation	ϕ	The bearing of the dune’s width-line.
Mean lee slope facing	ϕ_{lee}	Circular mean of φ in the steepest SS class area contained by the dune unit.
Crestline length	L_{crest}	The total length of the mapped crestline.
Crestline sinuosity	S_{crest}	The degree to which the dune’s crestline deviates from a straight line, represented with L_{crest}/W .
Interdune length	L_{id}	The smallest distance to the dune unit in the direction perpendicular to ϕ toward ϕ_{lee} . This was measured by casting rays from points every meter along the dune’s width-line.

4.5 Dune Geometric Characterization

The geometric characteristics we computed were based on characteristics described in (Baitis et al., 2014), which are based on a prototypical dune model. The characteristics that we measured for each dune unit are dune maximum height (h_{\max}), mean height (\bar{h}), perimeter (P), area (A), volume (V), circularity ratio (C), surface area (SA), width (W), length (L), orientation (ϕ), mean lee slope facing (ϕ_{lee}), crestline length (L_{crest}), crestline sinuosity (S_{crest}), and interdune length (L_{id}), which are described in Table 4.

The dune’s width line has been described as ”the visual best-fit straight line through the dune sinuosity” (Baitis et al., 2014). Lacking a means to characterize dune sinuosity by mapping the crestline without any orientation information, we formalized the width-line as the linear least squares regression line through the dune perimeter. We mitigated issues with predicting near-vertical best-fit lines by rotating the reference frame for the regression by 90° if the dune unit was longer in the y -dimension than the x . We translated the dune’s width-line so it passed through the dune unit’s centroid and truncated it to the extent of the projection of the dune unit’s perimeter onto the width-line.

We mapped the dune crestline from the highest-altitude points within a reference frame oriented such that the x -axis was parallel to ϕ . At every meter (the resolution of the dataset), we identified the maximum-altitude point along the entire width of the dune. We achieved the greatest semblance to manually-mapped crestlines when we omitted all points consisting of fewer than 5 contiguous samples within 5 m of each other, clipped the remaining segments of their end-points, and created a smooth pattern by interpolating with a third-order polynomial within the rotated reference frame. If segments were nearer than 10 m, we interpolated the width-line between them using a cubic Hermite spline. That is, we use a polynomial for congruent crestline segments and join adjacent crestline segments with a spline. The choice of technique to map and smooth the crestline undoubtedly influences measurements of crestline height, length, and sinuosity.

4.6 Dune Dynamics Characterization

We measured the net product of dune interactions (e.g., division, collisions, mergers) by computing a dune structure volatility index for each dune, which we characterized as the normalized ratio of the number of

spatially overlapping dune units between times t and $t + 1$, such that:

$$\psi(d_i) = \begin{cases} 2 \frac{|D_t|}{|D_t| + |D_{t+1}|} - 1, & \text{if } |D_t| > 0, \\ 0, & \text{otherwise,} \end{cases} \quad (7)$$

where D_{t+1} is the set of dunes in time step $t + 1$ which overlap the planimetric area of the dune of interest, d_i , in time step t by at least 50%, and D_t is the set of dunes in time step t with at least 50% overlap with dunes in D_{t+1} . We measured the degree of overlap as the larger of the fraction of dune unit i 's planimetric area occupied by dune unit j or that of j occupied by i . This structural volatility index spans the range [-1,1], where positive values suggest merging dune units, negative values suggest dividing dune units, 0 suggests that the local dune structure is stable between time steps, -1 indicates that no dunes exist in D_t , and 1 indicates that there is no related dune unit in D_{t+1} . Because we always assess from time t to $t + 1$, $\psi(d_i)$ is always > -1 . We did not analyze dunes where $\psi(d_i) = 1$ to avoid skew due to potential dune-mapping error. We expect overlap with at least the same dune units in the compared time steps, although movement and evolving shape of the dune body between time steps may move otherwise adjacent dune units into the overlap area. Each sampling by overlap will therefore tend to oversample dune units by about one additional dune-unit. That is, one dune in time step t will tend to overlap with two dune units in time step $t + 1$, and those two will tend to overlap with yet another dune unit in time step t . We therefore anticipate $D_t > D_{t+1}$ at an approximate 3:2 ratio, resulting in an expected bias in our volatility measurement of approximately +0.2.

For each pair of temporally adjacent dune maps, we measured dune horizontal migration by computing the mean and coefficient of variation of the width of the dune area mapped at time t that does not overlap with the dune area mapped at time $t - 1$ (that is, $D_t - D_{t-1}$), which measures dune migration on the lee side of the dunes. We omit measurements where the dune units at time t overlap $t - 1$ dune units in less than 50% of its area. This degree of overlap assumes that dunes have migrated less than half their length in the time between the compared datasets. We calculated sand flux as the product of each dune's mean height and the migration rate (after Ahmedou et al., 2007; Vermeesch and Drake, 2008; Davis et al., 2020).

We measured the dune field sediment budget as a function of the difference in altitude fields for each time comparison. For the differencing operations, we compared altitudes against a benchmark location within one White Sands National Park's parking areas south of the Alkali Flat trail head, which has a relatively fixed altitude and is located within all datasets' extents (32.818272°N, 106.27438°W).

As we expect dune field morphology to change in response to meteorological conditions, we used hourly wind, precipitation, and temperature data for the Holloman Air Force Base, located down-wind of the field area (KHMN, 32.85° N, 106.1° W; <https://mesowest.utah.edu/>, accessed 5 April 2022). We transformed these data to sum precipitation, monthly mean temperature, and theoretical sand flux (after Martin and Kok, 2017; Gunn et al., 2022b). We represented flux directionality as the ratio of resultant to absolute sand flux potential, which ranges from 0 (extreme variability) to 1 (unidirectional) and is similar to drift potential (i.e., RDP/DP; Gunn et al., 2022a; Fryberger and Dean, 1979). We related these conditions to dune morphological parameters and to dynamic parameters (migration rate, flux) to gain insight into dominant factors on dune field behavior.

5 Results

5.1 Validation and Filtering

Our dune-interdune classification is 92% accurate relative to our manual mapping (Table 5) and is weakest (at 90%) among parabolic dunes. The most consistent difference between the results of our approach and the manual mapping was a tendency for the automated mapping to slightly shorten the length of the dune on the stoss side relative to the manual mapping (Fig. 3). The lee edges tended to be highly precise to manual mapping. The division of the dune area into dune units appears to have been highly sensitive to subtle defects and micro-structures in the topography, resulting in more dune-unit boundaries than a human might have drawn depending on their criteria for identifying dune defects. This is particularly prevalent among the parabolic dunes which have rougher surface topography than barchanoid dunes (Fig. 3f).

Table 5: Confusion table comparing the results of our approach to manual mapping for each focus zones (a-f; Fig. 1). Units are in m². Reported precision is the "accuracy" of our approach in relation to manual mapping.

	a	b	c	d	e	f	total
True positive	1029644	860888	758515	1041877	984575	796501	5472003
False positive	31443	30205	16849	20737	21205	82201	202642
True negative	323856	471864	558057	296754	352850	491022	2494406
False negative	58995	80980	110516	84569	85307	74214	494584
Total area	1443939	1443939	1443939	1443939	1443939	1443939	8663636
Precision	93.74%	92.30%	91.18%	92.71%	92.62%	89.17%	91.95%

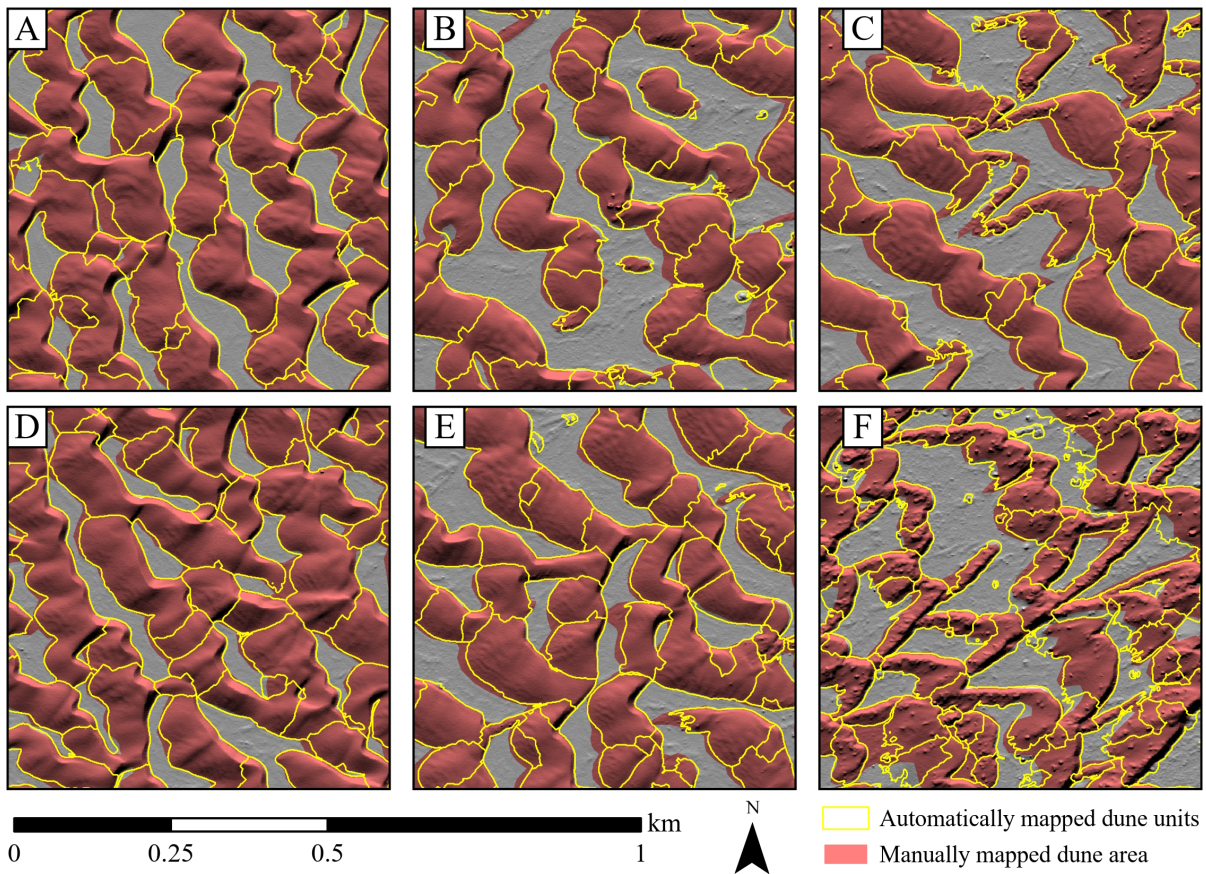


Figure 3: Comparison of manual mapping to automated mapping results for each zone (a-f) shown in Fig. 1. Images are zoomed in near the centers of each zone to show detail for comparison.

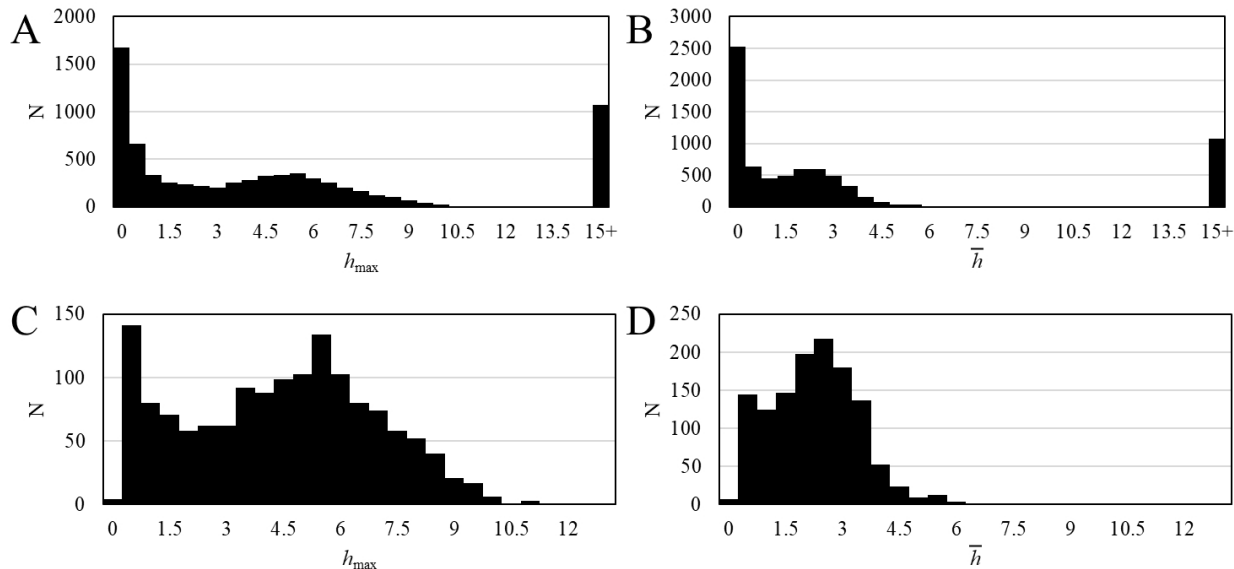


Figure 4: Dune height distributions: (A) maximum dune height without filters; (B) mean dune height without filters; (C) maximum dune height for dune units with maximum height <100 m, planimetric area >3000 m^2 , and volume <200000 m^3 ; (D) mean dune height with the same filters as (C).

It is inevitable in any computational model that erroneous results will be produced and some filtering may be required before any population-scale analysis can be undertaken. Importantly, we defined our filters to remove known issues or anomalies in the data and did not focus on achieving a prototypical dune boundary. We used Baitis et al. (2014) as a reference as to how to filter automatically-produced dunes to better compare to manual mapping results.

Our analysis divided the land surface into sections (dune and interdune) and further divided dune areas into individual dune objects. The boundaries between dune objects were chosen based on local decreases in dune volume and no direct limits were placed on dune object size. This process inevitably led to a large population of small dune objects, $< 2 \times 2$ DEM pixels, that don't themselves represent a dune feature. These often occurred at boundaries between larger dune objects, or in complex areas of dune interaction. This population of small, erroneous dune objects motivates an area filter, analyzing only dunes with planimetric areas >3000 m^2 .

Estimates of sub-dune topography were challenged in areas with substantial sand coverage, limited interdune areas, and near the edges of the dataset. Consequently, a substrate could not be accurately approximated in all areas, resulting in erroneous local and overall dune height measurements. Dune units with unreasonable heights (>100 m) and volumes (>200000 m^3) were therefore removed before assessing any measurements at the dune field scale. Parameters independent of the substrate interpolation (e.g., planimetric area) are reliable even where heights are miscalculated, however.

To illustrate the filtering approach, Figure 4 compares filtered and unfiltered dune heights. These plots demonstrate that the bulk of dunes showed reasonable heights between 1–8 m. These plots also show a substantial population of short (1–2 m) dunes. Nearly all small- h dune units physically relate to dune terminations or defects and vegetated dunes, including trailing arms and nebkhas. Few small- h dune units are erroneous and are typically associated with the margins of park roads. Filtered populations are compatible with prior manual work (Baitis et al., 2014), and weighting statistics by the dune volume gave weighted means that agree more closely.

We noted that the differences in mapping results between adjacent sub-datasets translated to sharp changes or "banding" in dune-unit characteristics in certain parameters, which are shown with the results of the respective parameters. These are principally due to the empirical clustering analysis done to define slope units, which constitute the most fundamental terrain unit we used for our mapping, which is exacerbated

by actual changes in dune field morphology from west to east across the dune field.

5.2 Mapping and Characterization

Each land-surface parameter and terrain unit component provided the spatial structure and context necessary to produce dune maps and dune-parameters that we used to evaluate dune field resilience. Slope angle (Fig. 5A) divided the land surface into steep lee slopes, gentle-to-moderate stoss slopes, and flat interdune. Slope azimuth (Fig. 5B) highlighted the distinction between east-facing lee slopes and west-facing stoss slopes, though both types of slopes spanned a range of slope azimuth. Consequently, the spatial relationships between slope-facet units based on natural divisions in slope angle and slope azimuth were necessary for coarser-scale contextualization necessary for mapping dune units. Slope azimuth varies at a higher spatial frequency in the interdune area than on dune surfaces. Mean curvature (Fig. 5C) highlighted convex areas on the land surface, particularly brinklines. Computing mean curvature with larger window sizes tended to mute small or narrow convex areas in the interdune area but also sometimes overgeneralized and overrepresented the extent of dune convexity, making it necessary to use a multiscale approach to filter convex areas and to use other parameters to provide important context for that convexity in order to map dunes. SACI highlighted dune boundaries and SADI highlighted dune crests (Fig. 5D), though both exhibited numerous small-scale defects due to the fuzzy nature of dune boundaries and crestlines, requiring altitude, slope angle, and slope azimuth for additional context in order to map dune units.

We mapped and characterized more than 18000 dune units across 8 datasets (Table 6). Our dune-interdune classification is 92% accurate to manual mapping (Table 5). Dune-unit boundaries reasonably define defects that terminate into interdune areas and interactions that terminate into other dunes (Fig. 6A-B). Boundaries between adjacent dune units also commonly occur in areas of high downwind convexity in the sinuosity (e.g., dune noses). This is likely due to constriction of the volume of the dunes at the points of high convexity. Some boundaries between adjacent dune units do not clearly represent identifiable dune elements. Small-scale relief structures had a negligible effect on the identification of dune-not dune boundaries, but did affect identification of dune boundaries between adjacent dune units that resulted in the excessive division of the dune area into dune units (Fig. 6C-D). The effect of small-scale relief structures on dune-unit boundaries was particularly evident in parabolic dunes, which exhibit complex surface morphology associated with vegetation, pedestals of (semi-)lithified sand, and blowouts (Figs. 6E-F, 7A-B). Overall, dune-unit divisions were highly aggressive in segmenting the dune area and dune units are consequently generally smaller than dunes mapped manually in previous studies (e.g., Baitis et al., 2014), and small relief variations sometimes cause significant boundary changes across time. Consequently, and in conjunction with dune migration, the number of dune units within any particular zone may fluctuate significantly with time (Table 6) and the statistical reduction of dune-unit characteristics is therefore generally more reliable than specific dune-unit boundaries.

Dune crestlines were mapped as lines connecting points of the maximum elevation in repeated transects perpendicular to the dune width-line. These lines were often discontinuous, as well-defined crestline does not always exist (Figs. 7C; 8). Our crestlines differed significantly from prototypical dune crestlines, which are typically manually digitized in 2D images continuously along the approximate highest point approximately perpendicular to the gross orientation of the dune and the local brinkline (e.g., Ewing et al., 2006). Consequently, our dune crestline mapping does not compare well to previous work.

5.3 Dune Field Characteristics

5.3.1 Height

Dune height is useful for validation and data filtering, and we observed variations in dune height across the dune field. Mean dune height across all datasets is 6.56 m (standard deviation 1.93 m). Dunes are distinctly taller in the westernmost and east-central portions of the dune field, with yearly averages ranging between 6.0 and 8.9 m tall (Fig. 9). The shortest dunes (yearly averages ranging between 5.0 and 6.9 m tall) were located in zones of relatively sparse barchanoid dunes, where we also noted sparse vegetation (areas b and c). There is no clear pattern of dune height changing with time or with respect to dune type (Table 7; Fig. 11A).

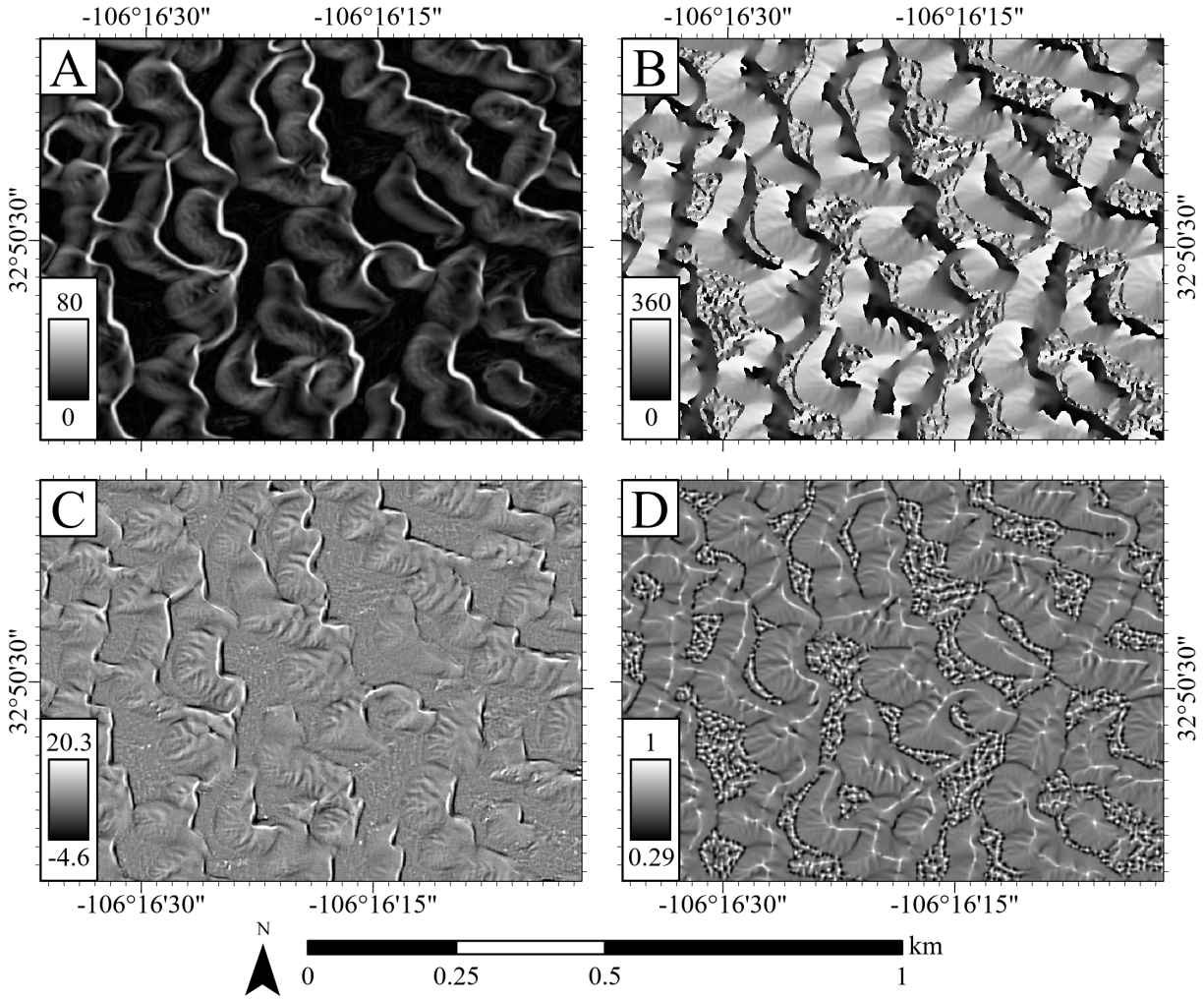


Figure 5: Land-surface parameters used for topographic analysis at White Sands National Park, New Mexico: (A) slope angle, (B) slope azimuth, (C) mean curvature ($\times 100$ scaling factor), (D) slope-azimuth divergence index (SADI). These land-surface parameters were used to extract basic terrain units and evaluate dune field morphology to map and characterize sand dunes. Note the distinctive patterns in slope angle and slope azimuth that highlight lee slopes, the areas on dune crests and brinklines highlighted by mean curvature, dune crests highlighted by SADI, dune boundaries highlighted by convergence (low-SADI areas), and the difference in spatial frequency of slope-azimuth and SADI variability between dune slopes and the interdune plain.

Table 6: Number of dune units with each dataset and within each zone (a–f) indicated in Figure 1. Dunes with physically unreasonable geometry ($h_{\max} > 100$ m, $A < 3000$ m², or $V > 200000$ m³) are omitted. Please note that the 2015, 2018, and 2020 datasets are larger than the earlier datasets, resulting in more dune units mapped in those years, and that dunes migrate in and out of the smaller study zones. Dune-unit boundaries are sensitive to microvariations in topographic structure, which evolves constantly in an aeolian setting and is reflected in the fluctuating count of dune units.

Date	global	a	b	c	d	e	f
2007 June	1906	62	62	70	75	76	88
2008 June	1987	71	60	72	92	85	57
2009 January	2029	73	78	56	88	90	95
2009 September	1996	69	73	67	76	81	92
2010 June	1931	70	67	69	76	75	80
2015 August	2378	70	54	59	79	70	87
2018 December	3370	98	53	48	71	47	88
2020 January	2533	63	58	71	0	0	0
Total	18130	576	505	512	557	524	587

Table 7: Results from ordinary least squares reduction of dune units with respect to time. Note that dune units from the June 2007 dataset are omitted for dune velocity and sand flux, as these characteristics were measured using backward finite differencing. All relationships were found to be statistically significant.

Characteristic	Units	N	intercept	slope [day ⁻¹]	p
h_{\max}	[m]	18130	6.3487	0.0001	0.0000
\bar{h}	[m]	18130	2.8563	0.0000	0.0000
w	[m]	18130	151.5658	0.0025	0.0000
L	[m]	18130	53.0863	0.0007	0.0000
A	[m ²]	18130	8522.2248	0.3064	0.0000
V	[m ³]	18130	25376.3730	1.4614	0.0000
A/SA	unitless	18130	0.9802	0.0000	0.0002
C	unitless	18130	0.2918	0.0000	0.0000
Migration Rate	[m yr ⁻¹]	14795	3.3644	-0.0001	0.0000
Sand Flux	[m ² yr ⁻¹]	14795	9.5025	-0.0004	0.0000

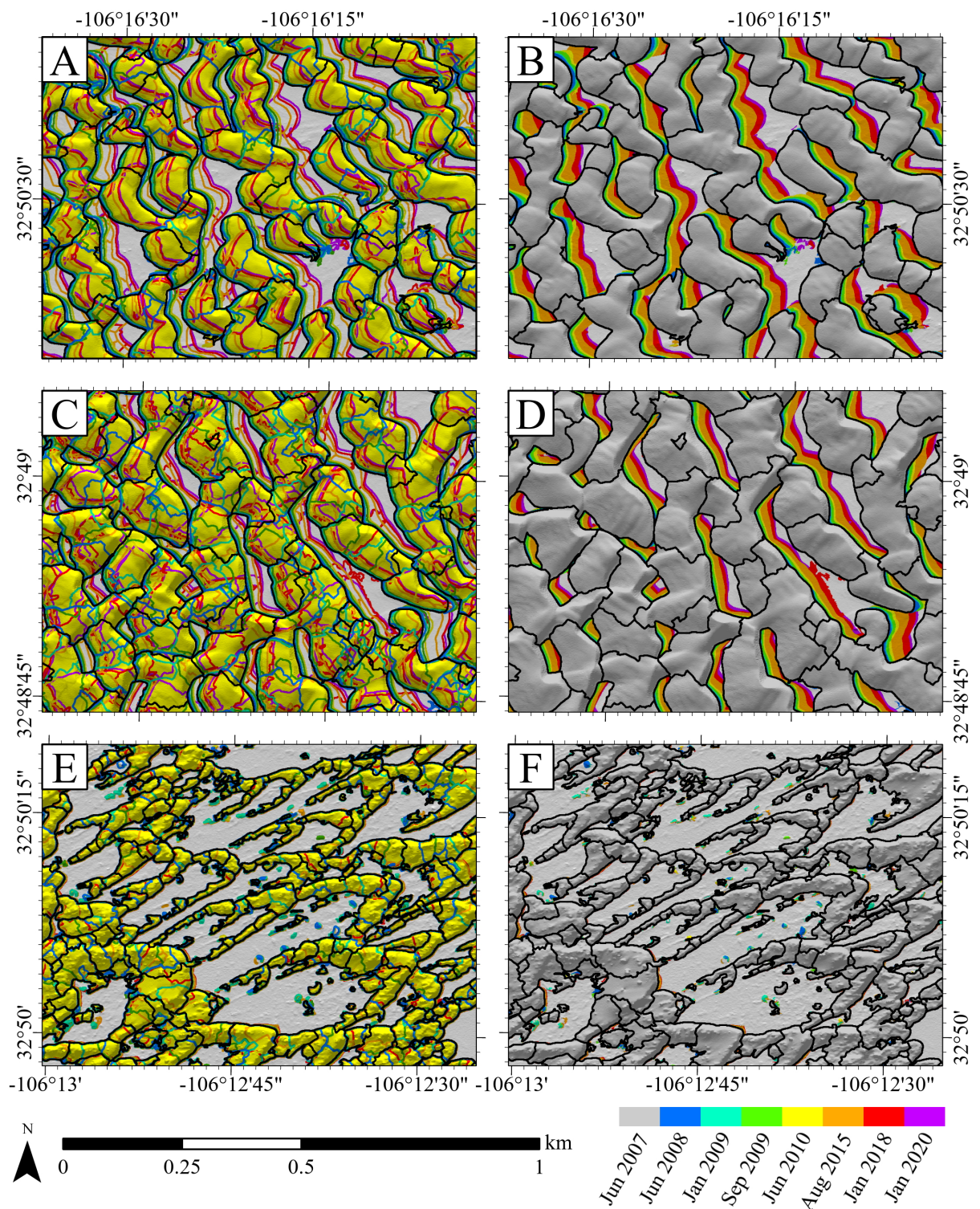


Figure 6: Dune units, with the dune units of each temporal dataset shown with colored outlines (left) and progressive fill (right): (A-B) typical dunes located in the north-central part of the study area; (C-D) tightly-spaced dunes located in the southwestern part of the study area; (E-F) Parabolic dunes, which exhibit complex surface morphologies that resulted in a high degree of dune unit division.

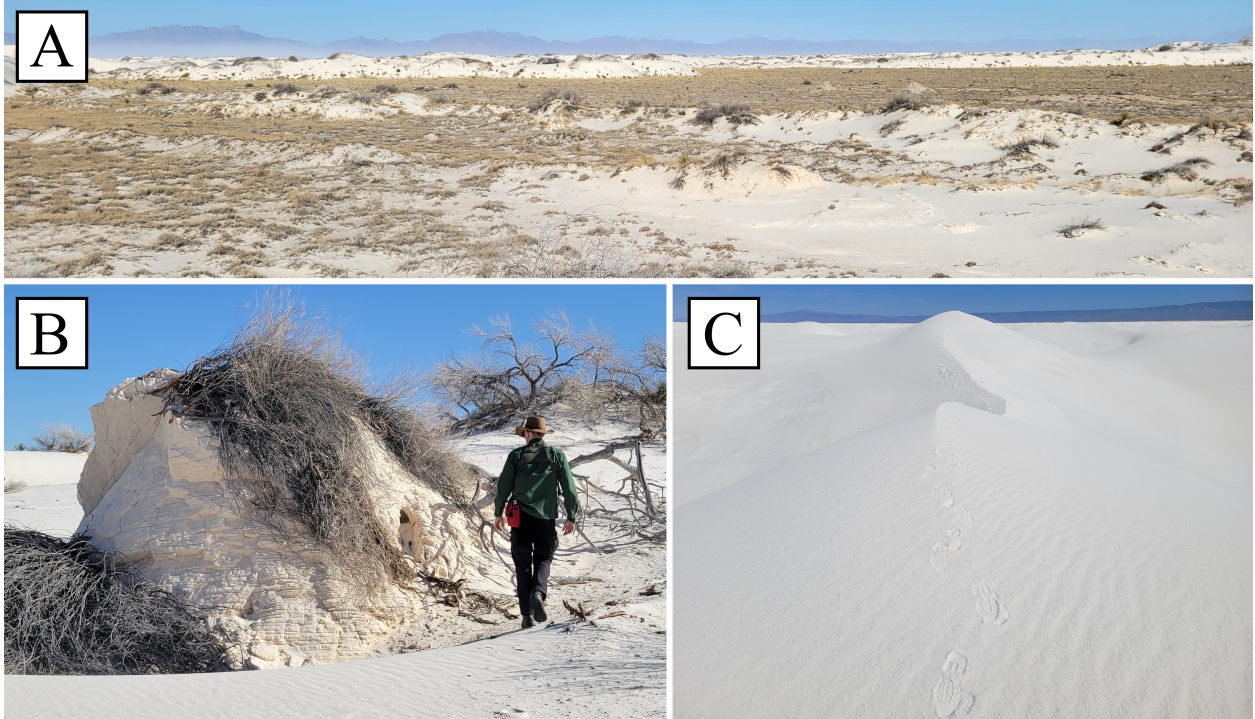


Figure 7: Examples of departures from to ideal dune morphology and semantics: (A) a small parabolic dune exhibiting mounds, nebkhas, and sand blowout, (B) a pedestal that represents a small-scale, non-dune eminence, and (C) disappearance of a distinct morphological crestline.

5.3.2 Width and Length

Mean dune width and length across all datasets are 156.93 m (standard deviation 68.22 m) and 54.67 m (standard deviation 15.50 m), respectively (Fig. 11B–C). Dune width and length trend slightly toward larger dunes over time at a rate of 0.91 and 0.26 m yr⁻¹, respectively (Table. 7). Parabolic dune width is shorter than barchanoid dunes (mean 133.00 m) due to the over-division of parabolic dune units caused by their surface morphology. The length of parabolic dunes is also narrower than that of barchanoid dunes (mean 45.19 m), consistent with their morphology.

5.3.3 Area and Volume

Dune units occupied a mean footprint of 9177.17 m² and mean volume of 28500.00 m³ across all datasets (Fig. 11D–E), with considerable variability (standard deviations 6334.19 m² and 324788.88 m³, respectively). Parabolic dune units occupy notably smaller areas than barchanoid dunes, which is partially due to their complex surface morphology that results in numerous small dune units mapped for each parabolic dune. Mean dune area and volume appear to have a subtle tendency toward larger dunes over time, at a rate of 111.91 m² day⁻¹ and 533.78 m³ day⁻¹, respectively (Table 7).

5.3.4 Area/Surface Area Ratio

The planimetric area-surface area ratio is a measure of object-scale relief, where smaller values indicate generally more rapid relief gain over the unit’s area. Parabolic dunes have distinctive high relief, with mean A/SA of 0.967 over their area for all datasets compared to barchanoid dunes, which have mean A/SA of 0.980 (Fig. 12). Relatively flat barchanoid dunes, with greater ratio values, broadly occur in the same areas as short dunes, where there is sparse vegetation (Fig. 11F). There does not appear to be significant change in A/SA over the observed time period (Table 7).

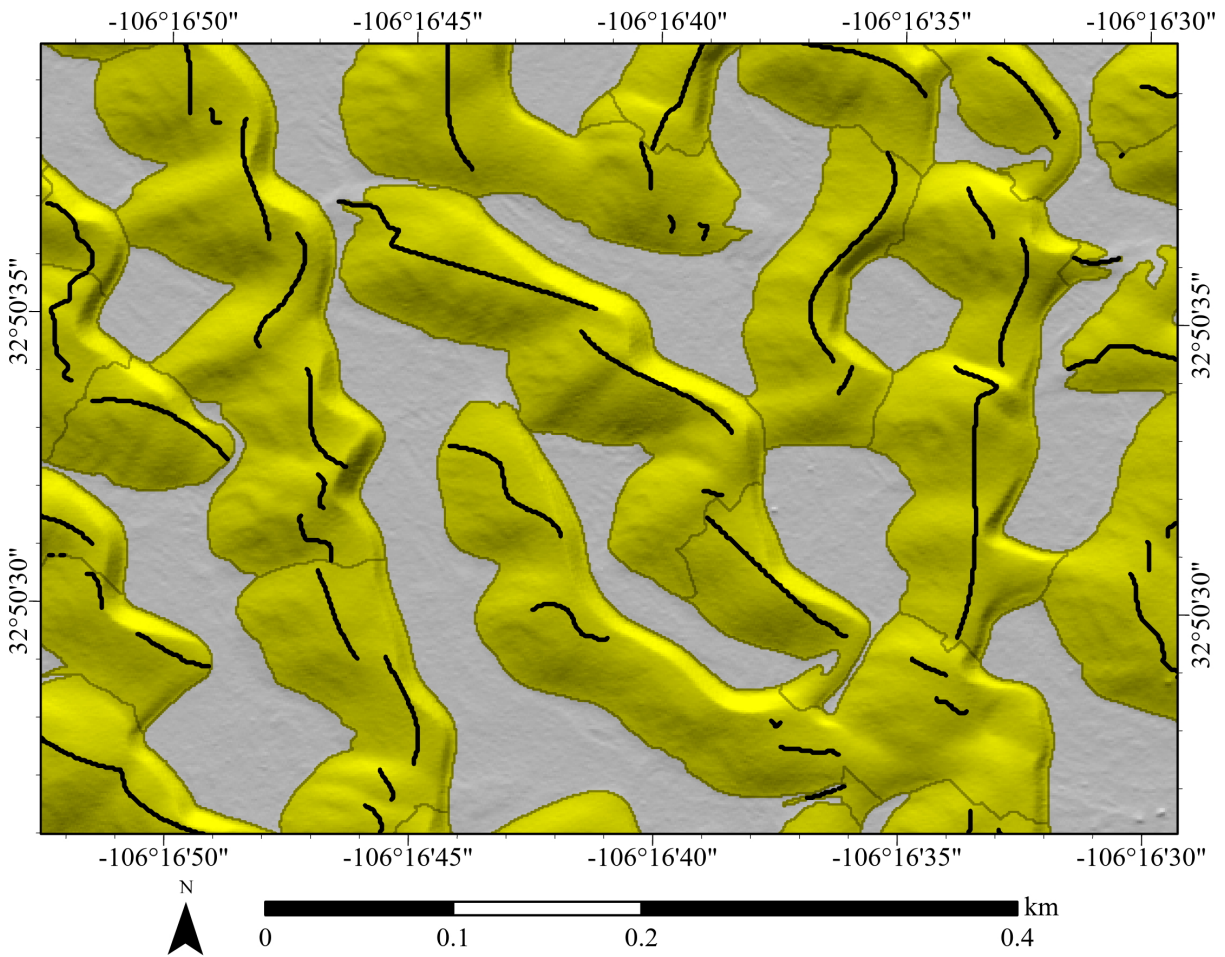


Figure 8: Example dune crestlines (black lines) mapped on dune units (yellow). Crestlines are mapped as the string of maximum-altitude points within a dune unit in a series or transects oriented perpendicular to the dune unit's width-lines. Note that this conceptualization of dune crest is insufficient for mapping continuous crest-lines, requiring additional smoothing and resulting in many disjoint crestlines. Where crests are very disjointed, no crestline could be mapped.

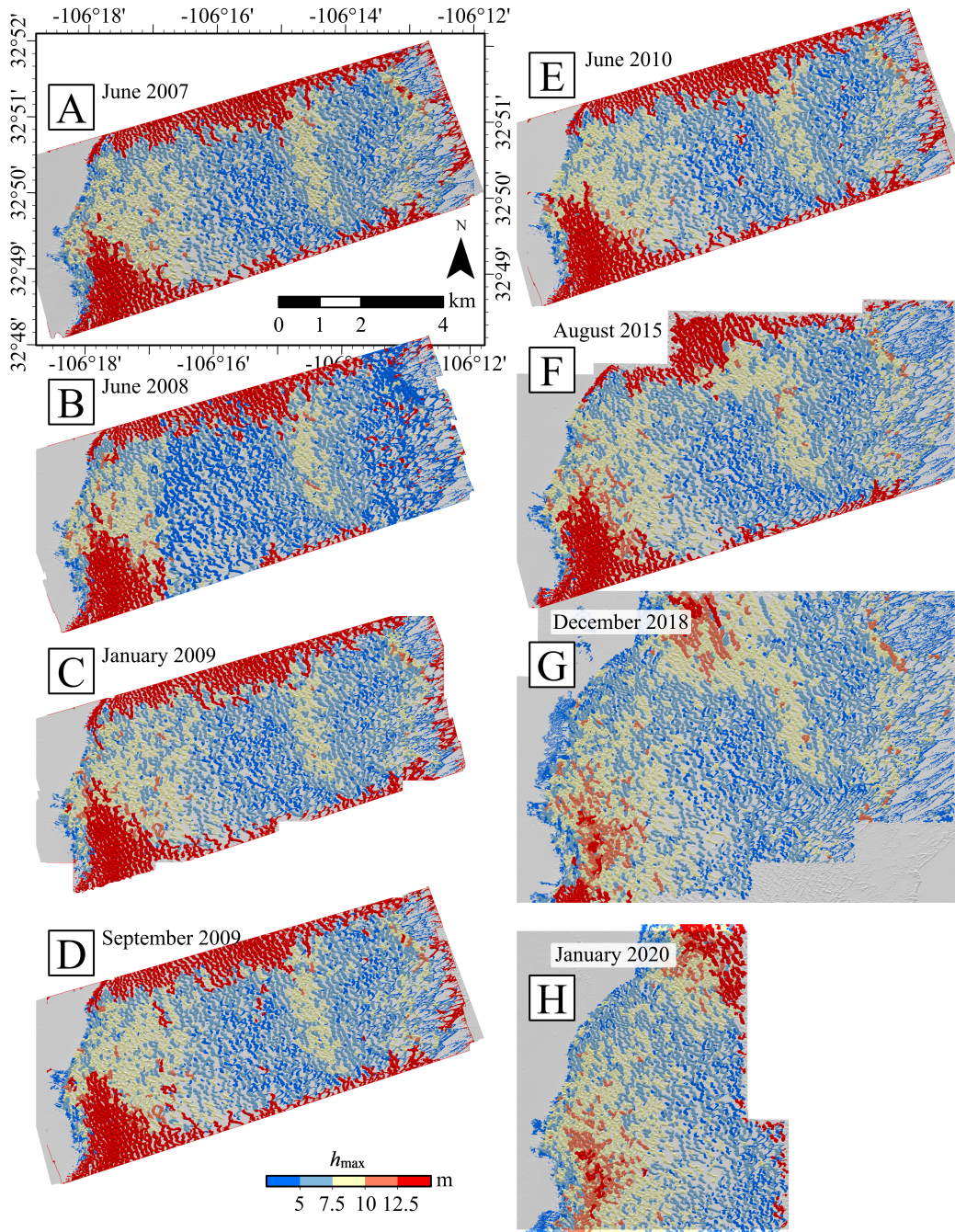


Figure 9: Dune height for each of (A) June 2007, (B) June 2008, (C) January 2009, (D) September 2009, (E) June 2010, (F) August 2015, (G) December 2018, and (H) January 2020. The category of dune units exceeding 12.5 m (red) exhibit very large height values (i.e., in excess of 100 m) due to substrate interpolation error and were omitted from further analysis.

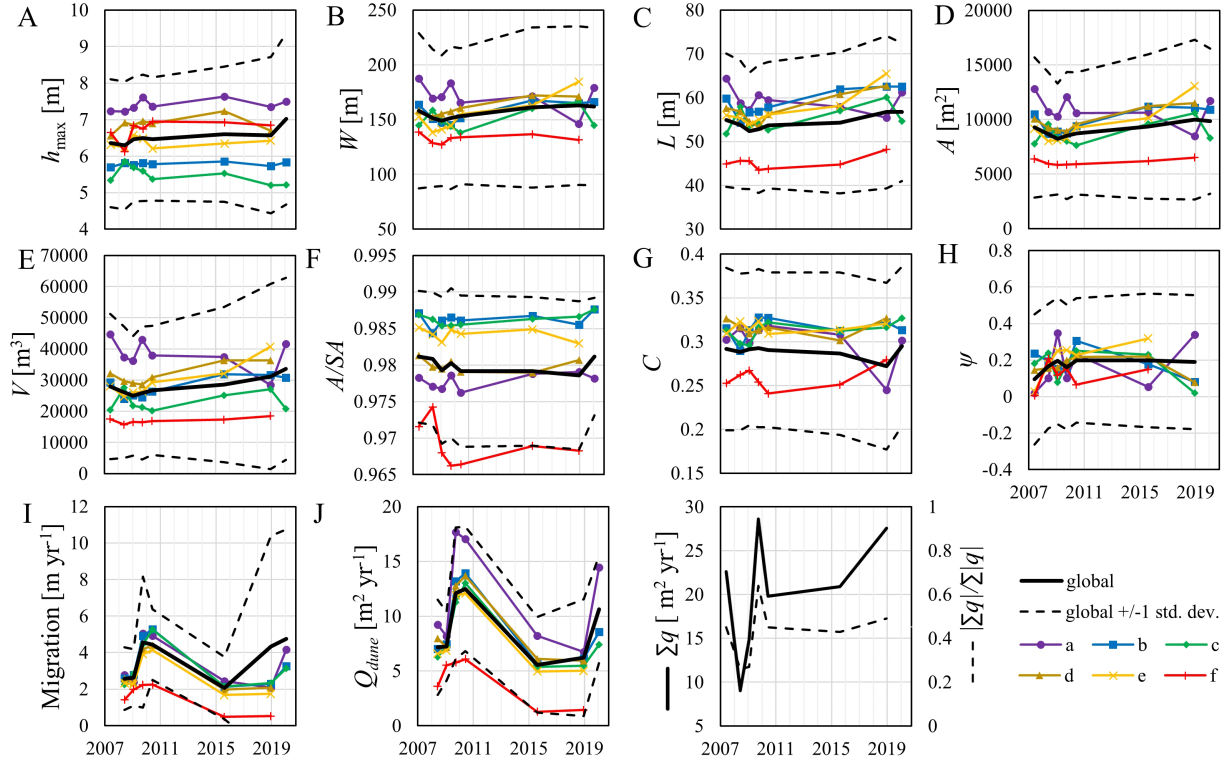


Figure 10: Spatial reduction and temporal evolution of dune unit characteristics and dynamics globally and within each zone indicated in Figure 1: (A) height, (B) width, (C) length, (D) planimetric area, (E) volume, (F) area-surface area ratio, (G) shape-circularity ratio, (H) structural volatility index, (I) migration rate, and (J) sand flux estimated from dune migration rate and height. For comparison, we include (K) potential sand flux ($\sum q$) and flux directionality ($|\sum q|/\sum |q|$) estimated from wind data measured at the Holloman Air Force Base (KHMN). Dunes with physically unreasonable geometry ($h_{\max} > 100$ m, $A < 3000$ m², or $V > 200000$ m³) are omitted. Note the distinctive morphometry that separates parabolic dunes in zone f from barchanoid dunes in the rest of the study area. Also note the relatively high flux rates in 2009–2010. The apparently high migration and flux rates in 2018–2020 are primarily due to the omission of the eastern, slower portion of the study area in the 2020 dataset.

Figure 11: Spatial reduction and temporal evolution of dune unit characteristics and dynamics globally and within each zone indicated in Figure 1: (A) height, (B) width, (C) length, (D) planimetric area, (E) volume, (F) area-surface area ratio, (G) shape-circularity ratio, (H) structural volatility index, (I) migration rate, and (J) sand flux estimated from dune migration rate and height. We also include (K) potential sand flux estimated from the sa. Dunes with physically unreasonable geometry ($h_{\max} > 100$ m, $A < 3000$ m², or $V > 200000$ m³) are omitted. Note the distinctive morphometry that separates parabolic dunes in zone f from barchanoid dunes in the rest of the study area. Also note the relatively high flux rates in 2009–2010. The apparently high migration and flux rates in 2018–2020 are primarily due to the omission of the eastern, slower portion of the study area in the 2020 dataset.

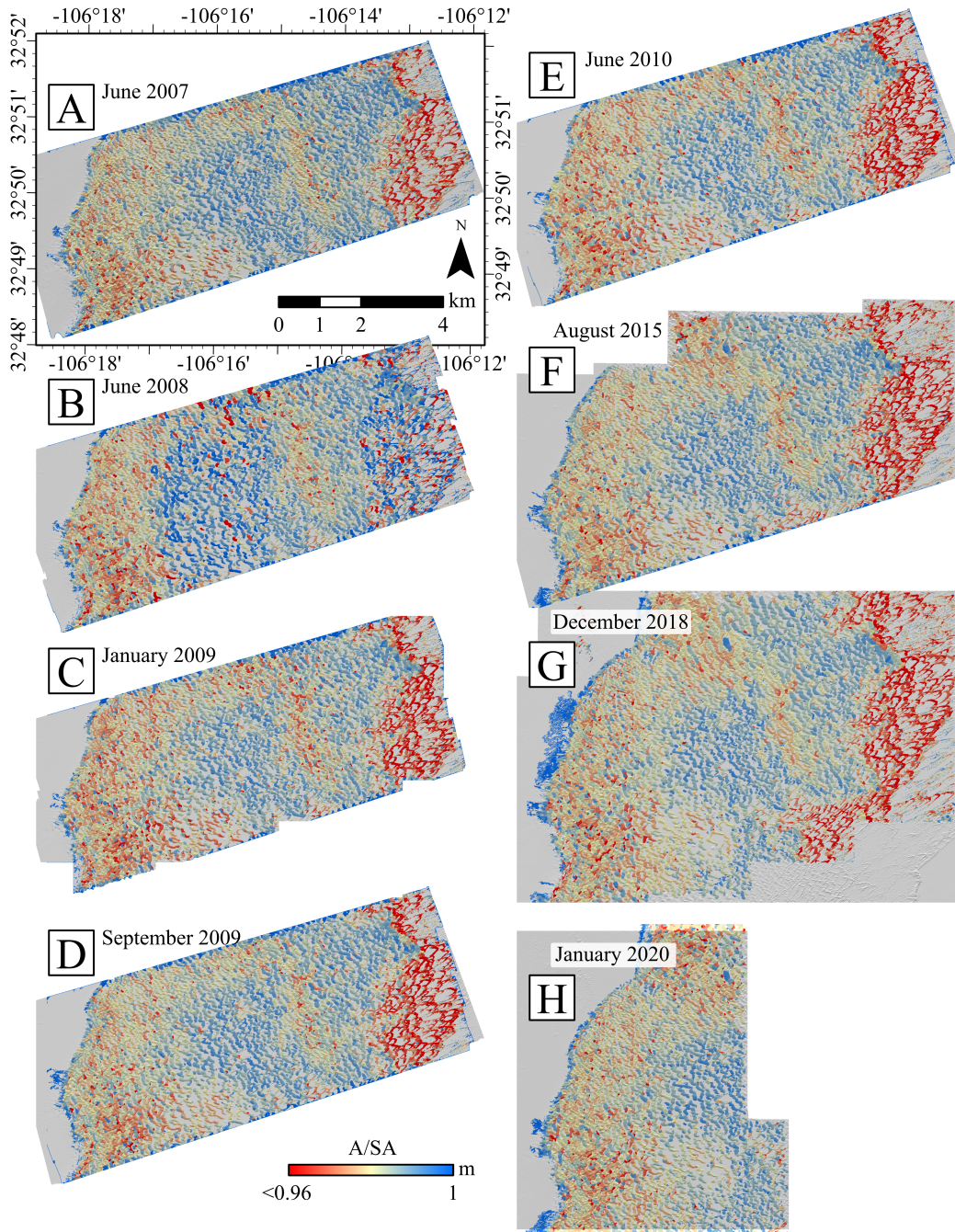


Figure 12: Dune planimetric-to-surface area ratio for each of (A) June 2007, (B) June 2008, (C) January 2009, (D) September 2009, (E) June 2010, (F) August 2015, (G) December 2018, and (H) January 2020. Note that parabolic dunes tend toward the lowest ratio values, indicating relatively high relief over their area, and the relatively low relief or flatter barchan dunes in the central and eastern portions of the dune field.

5.3.5 Circularity Ratio

Parabolic dunes are visually distinct by their narrow, curved shape compared to barchan dunes which have generally ovoid footprints except for their horns. Despite aggressive dune-unit division among parabolic dunes, dune units on parabolic dunes are distinctly non-circular, or spatially less-compact, with mean C 0.25 compared to barchanoid dune units with mean C of 0.291 (Fig. 11G). Dune circularity does not appear to significantly decrease slightly with time (Table 7).

5.3.6 Orientation

Dune units are predominantly oriented north-south or east-west (Fig. 13). This dichotomy appears to be due to aggressive dune disaggregation, resulting in dune units whose long axes reflect on typical orientations of each barchan horn, rather than the entire barchan. East-west-oriented dune units are more common in the east and in the south-central part of the area, coincident with shorter dunes, parabolic dunes, and sparse vegetation.

Compared to dune unit width-line orientations, lee slope orientations are more consistently toward the northeast, although other orientations are common in the east and south-central parts of the area, as with dune unit orientation (Fig. 14). Because lee slope identification depends on the classification of slope-facet units, and those are dependent on the global distribution of slope-angle and slope-azimuth, some areas exhibit greater variability in lee slope orientation than others as an effect of sub-dividing each dataset prior to processing.

5.3.7 Other Characteristics

We found all dune wavelength and interdune measurement characteristics to be invalid. This was due to conceptual and semantic issues in their measurement that were not resolved in this study. We chose to measure inter-dune distances as the minimum distance cast from all points along the dune width-line to the nearest dune unit in the dune's forward direction (the direction of its lee slopes), but this was problematic because adjacent dune units will often register as the nearest next dune, rather than a dune one wavelength away.

5.4 Dune Field Dynamics

5.4.1 Structural Volatility

Dune unit boundaries are influenced by small differences in relief structure which are not always related to prototypical dune-unit boundaries, causing incongruity between spatially overlapping or temporally adjacent dune-unit maps that indicates considerable uncertainty in the context of dune-pattern evolution. This is demonstrated by a standard deviation of the structural volatility index that is large in comparison to the total range of the index (0.339). Dune structure appears to be stable with time (Fig. 11H) with a mean structural volatility index of 0.201 across all time comparisons. This slightly positive value was anticipated as a sampling bias that would potentially yield a larger number of dune units at time t compared to time $t + 1$ —on average, three dune units at time t compared to two dune units at time $t + 1$. Accounting for that bias, there appears to be no tendency toward dune unit division or aggregation with time.

5.4.2 Dune Migration and Flux

The mean dune migration rate across all time comparisons was 3.65 m yr^{-1} (standard deviation 4.09 m yr^{-1}) (Fig. 11I), with a mean coefficient of variation per-dune of 0.41 (standard deviation 0.14). Migration rate tends to decrease eastward across the dune field, with relatively low migration in the sparsely vegetated central and eastern portions of the dune field and minimal migration among parabolic dunes at $<1 \text{ m yr}^{-1}$ (Fig. 15). The period from January 2009 to June 2010 exhibits abnormally high migration rates, with mean rate of 4.57 m yr^{-1} from January–September 2009 and 4.44 m yr^{-1} from September 2009–June 2010, and often in excess of 5 m yr^{-1} . Migration from 2015–2018 and 2018–2020 is comparable, with respective means of 4.34 and 4.67 m yr^{-1} . The slower years exhibit mean migration rates of 2.58 , 2.64 , and 2.07 m yr^{-1} (2007–2008, 2008–2009, and 2010–2015, respectively).

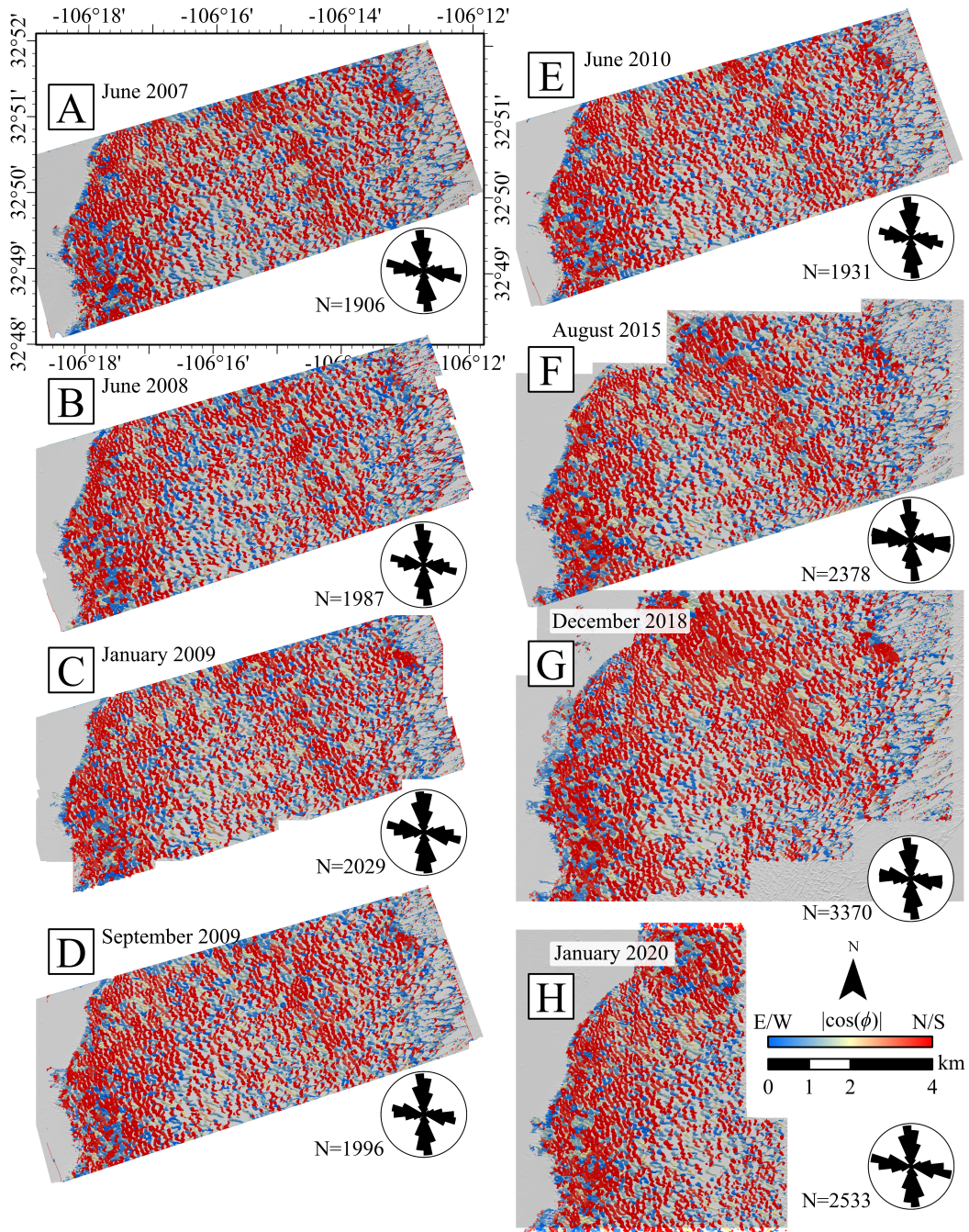


Figure 13: The orientation of the dune width-line for each of (A) June 2007, (B) June 2008, (C) January 2009, (D) September 2009, (E) June 2010, (F) August 2015, (G) December 2018, and (H) January 2020. Dunes with physically unreasonable geometry ($h_{\max} > 100$ m, $A < 3000$ m², or $V > 200000$ m³) are omitted from the rose diagram reductions.

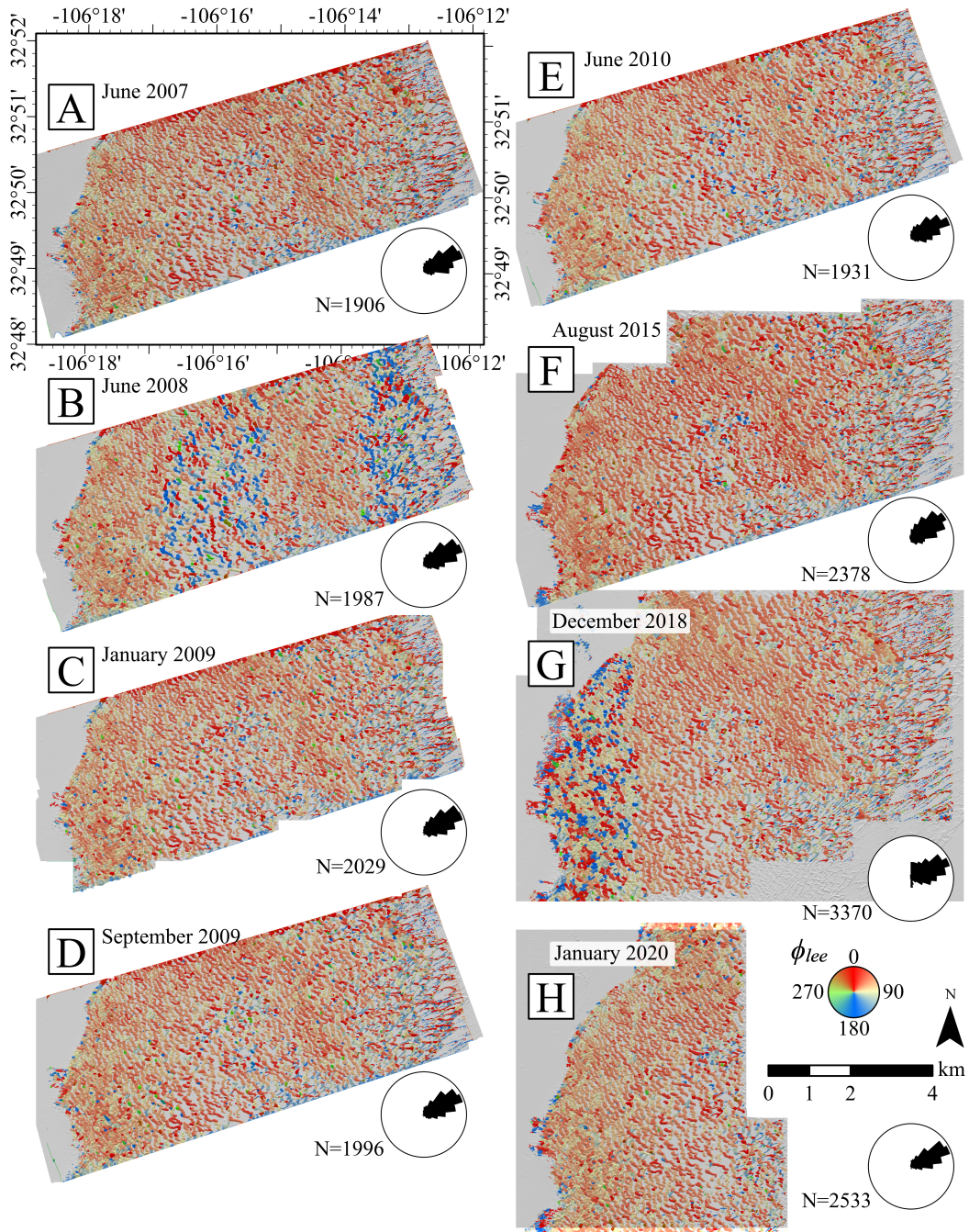


Figure 14: The mean orientation of each dune’s lee slopes for each of (A) June 2007, (B) June 2008, (C) January 2009, (D) September 2009, (E) June 2010, (F) August 2015, (G) December 2018, and (H) January 2020. The effects of processing sub-areas are manifest in (B) and (G), due to differences in the statistical distribution of land-surface parameters between sub-areas that resulted in different slope-facet categories and dune-unit boundaries, some of which tended toward greater capture of southward-facing steep slopes (i.e., on barchan horns, transverse noses, convexities, or longitudinal defects). Dunes with physically unreasonable geometry ($h_{\max} > 100$ m, $A < 3000$ m², or $V > 200000$ m³) are omitted from the rose diagrams.

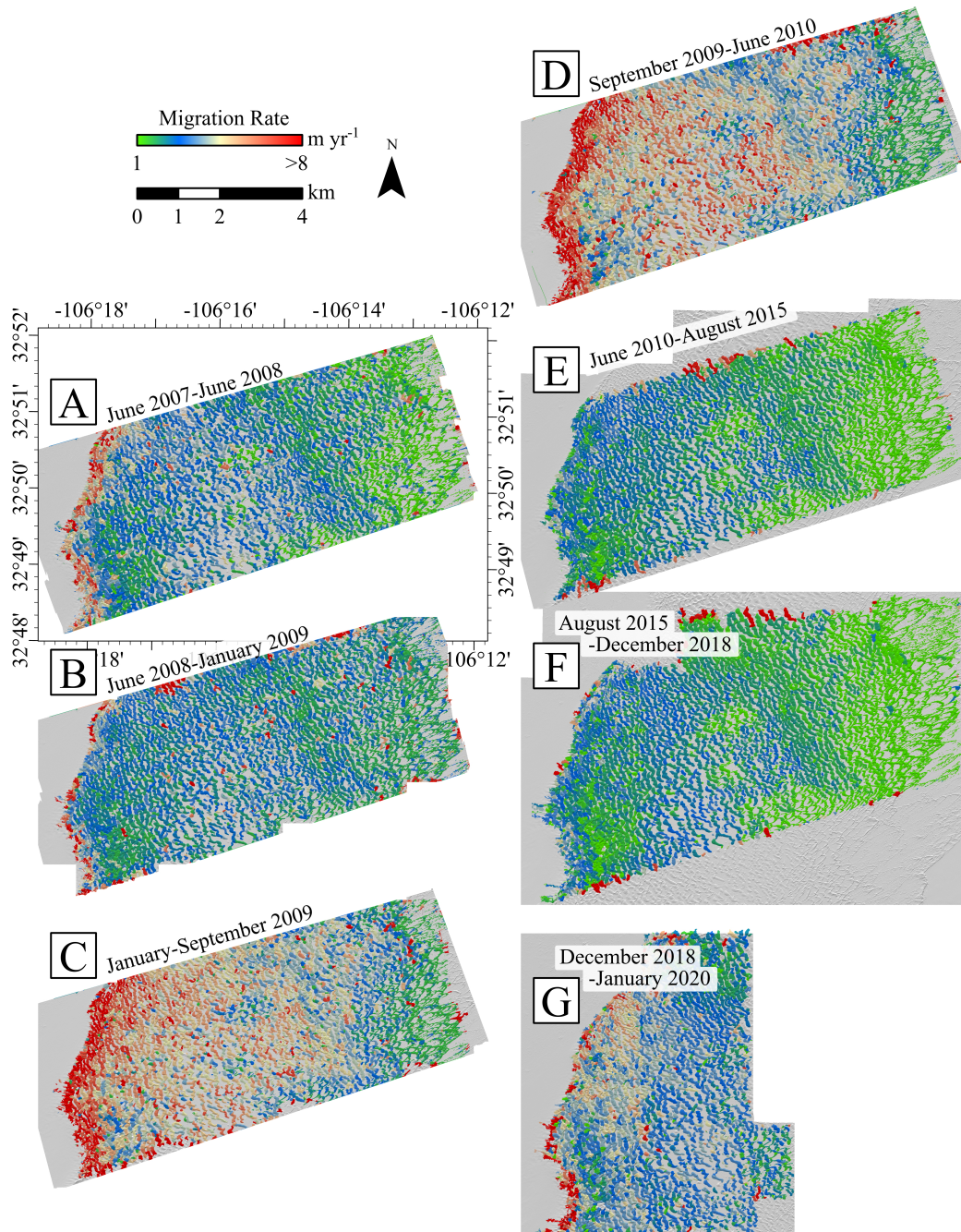


Figure 15: Dune migration rate from (A) June 2007 to June 2008, (B) June 2008 to January 2009, (C) January 2009 to September 2009, (D) September 2009 to June 2010, (E) June 2010 to August 2015, (F) August 2015 to December 2018, and (G) December 2018 to January 2020. Note the variability in migration rate from rapid years (2009; C–D) to slow years (2010–2018, E–F).

Table 8: Global mean DEM differencing results, ± 1 standard deviation. $\Delta V/\Delta t$ and $\Delta M/\Delta t$ are the volume and mass differences with respect to time. We assume an average bulk density of 1465 kg m^{-3} (Watkins et al., 1972). Note that each comparison only includes data contained within both compared datasets and that each comparison may vary in extent from other comparisons. Also note that the overall difference in sand volume in all sets of overlapping regions is near-zero.

Begin Date	End Date	N	mean [mm]	$\Delta V/\Delta t$ [$\text{mm m}^2 \text{ yr}^{-1}$]	$\Delta M/\Delta t$ [kg yr^{-1}]
2007 June	2008 June	45526348	12.95 ± 429.78	12.92 ± 415.69	18.93 ± 627.91
2008 June	2009 January	43185208	11.95 ± 261.94	18.40 ± 403.41	26.95 ± 590.99
2009 January	2009 September	43413491	-14.16 ± 406.96	-21.27 ± 611.27	-31.16 ± 895.51
2009 September	2010 June	45684601	25.80 ± 556.65	36.93 ± 796.77	54.10 ± 1167.27
2010 June	2015 August	45703634	-37.29 ± 1379.68	-7.21 ± 266.59	-10.56 ± 390.55
2015 August	2018 December	57227295	13.28 ± 1007.47	3.97 ± 301.42	5.82 ± 441.57
2018 December	2020 January	44213564	20.13 ± 529.14	18.18 ± 478.06	26.64 ± 700.36
2007 June	2020 January	26430135	21.98 ± 2776.47	1.74 ± 219.64	2.55 ± 321.77

Sand flux computed from dune height and migration rate exhibit the same spatial and temporal patterns as migration rate, with mean flux across all datasets of $8.50 \text{ m}^2 \text{ yr}^{-1}$ or $0.39 \text{ g m}^{-1} \text{ s}^{-1}$, and peak mean flux in 2009 of $12.09 \text{ m}^2 \text{ yr}^{-1}$ or $0.56 \text{ g m}^{-1} \text{ s}^{-1}$ (Figs. 11J, 16).

5.4.3 Dune Field Sediment Budget

The net change that we observed using DEM differencing, evaluated for all locations in the dune field regardless of dune presence, tends to be near-zero ($<40 \text{ mm yr}^{-1}$; Table 8). The dune field exhibits a net positive balance of 1.74 mm yr^{-1} ($2.52 \text{ kg m}^{-2} \text{ yr}^{-1}$) from June 2007 to January 2020.

The most rapid changes in the sediment budget are a net loss observed from January to September 2009 balanced by a net gain from September 2009 to June 2010 (-14 and 26 mm , or 31 and 54 kg yr^{-1} , respectively; Table 8). The dichotomous 2009–2010 sediment budget reflects significant seasonality, where summer and autumn easterly and northerly winds bevel sand dunes, and strong winter and spring southwesterly winds resupply the dune field with sediment from Lake Otero sediments (Kocurek et al., 2007; Jerolmack et al., 2011; Eastwood et al., 2012; Ewing et al., 2015; Swanson et al., 2016).

5.4.4 Weather Characteristics

Predominant southwesterly winter and spring winds drive northeastward sand flux, with much weaker north-northeasterly winds and less flux in the summer and autumn months (Fig. 17). The net flux potential for the study area from July 2007 to January 2020 is northeastward at $0.96 \text{ g m}^{-1} \text{ s}^{-1}$, with a directionality ratio of 0.44 (Fig. 18A). The relatively slow migration period prior to September 2009 exhibited highly variable flux (0.14 – 0.22), and the magnitude of flux reached its lowest point of $0.42 \text{ g m}^{-1} \text{ s}^{-1}$ in the period from 2008 to 2009, followed by $0.69 \text{ g m}^{-1} \text{ s}^{-1}$ from January to September 2009 (Fig. 18B–D). Flux potential peaked in the period from September 2009 to June 2010 at $1.33 \text{ g m}^{-1} \text{ s}^{-1}$, which was accompanied with the least variable flux (0.64) of the studied periods (Fig. 18E) and rapid dune migration rates. The slow-migration period following 2009–2010 is marked by average-magnitude flux potential and variability (0.92 – $0.97 \text{ g m}^{-1} \text{ s}^{-1}$ and 0.43 – 0.45 , respectively; Fig 18F–G) which was followed by a high-flux potential period from 2018 to 2020 (flux $1.28 \text{ g m}^{-1} \text{ s}^{-1}$ and variability 0.49 ; Fig. 18H).

The study area experienced bouts of precipitation exceeding 300 mm in July 2007 and May 2010, and months exceeding 600 mm in 2011 and 2012, followed by a dry period through 2020 (Fig. 19). The rapid migration event in 2009 occurred about two years after the 2007 rainfall, followed by slow migration after the unusually intense 2011–2012 rainfall.

A combination of higher winter temperatures combined with low winter and summer dew point temperatures in 2009 appears to be coincident with the rapid 2009 migration rates, followed by high winter and summer dew point temperatures coincident with the slow 2010 migration rates, but we did not identify other relationships between temperature and dune field behavior (Fig. 19).

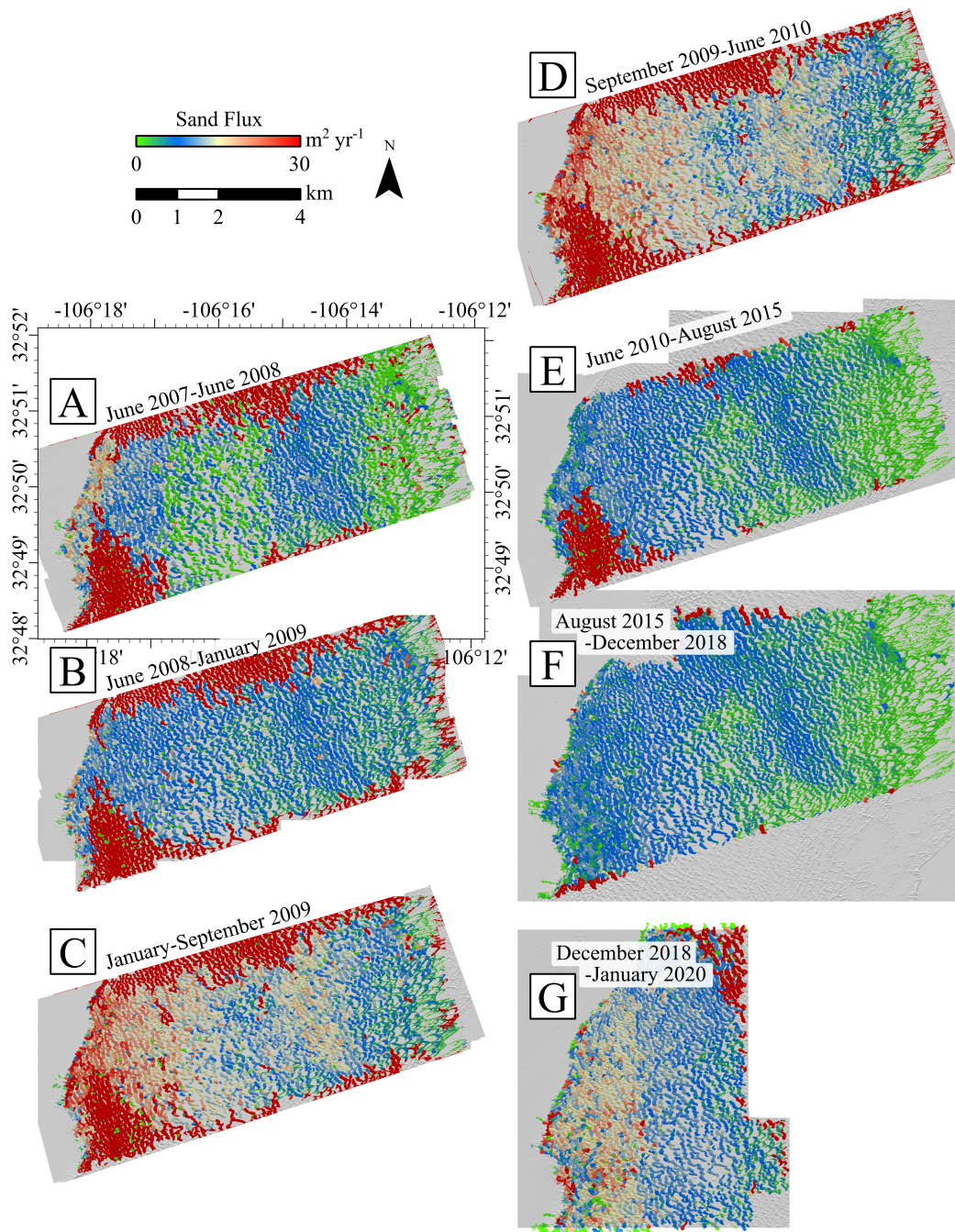


Figure 16: Dune sand flux from (A) June 2007 to June 2008, (B) June 2008 to January 2009, (C) January 2009 to September 2009, (D) September 2009 to June 2010, (E) June 2010 to August 2015, (F) August 2015 to December 2018, and (G) December 2018 to January 2020. The vertical discontinuity accentuated in G is due to differences in the statistical distribution of land-surface parameters between sub-areas that resulted in slightly different patterns of slope-facet categories and dune-unit boundaries than other portions of the study area for that time period.

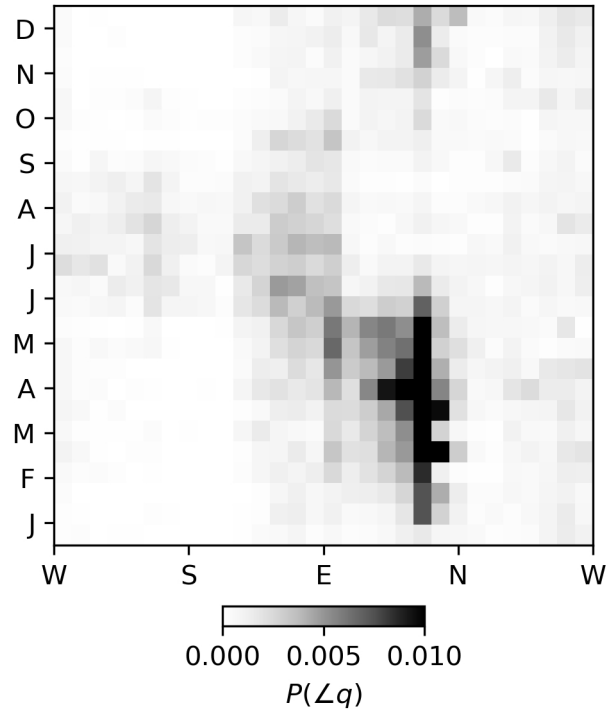


Figure 17: Directionality of sediment flux from July 2007 to January 2020, estimated from hourly wind data measured at the Holloman Air Force Base (KHMN). Southwesterly winter and spring winds primarily drive northeasterly flux.

6 Discussion

6.1 Geomorphometry of Dune Mapping

Our dune mapping represents a mathematic formalization of a conceptual model of dune topographic structure, including dune boundaries and the relationships between dunes and geomorphometric parameters. We have demonstrated that a structural approach is effective for mapping sand dunes, and have observed spatial and temporal variations of dune characteristics in detail. Opportunity exists to advance geomorphological mapping through semantic modeling to represent conceptual models within a quantitative framework.

The most critical land-surface parameters in our analysis were altitude, slope-angle, and slope-azimuth. Altitude was the ultimate differentiator between dune and interdune, where the concept of separateness in a statistical context was particularly helpful. Slope-angle and slope-azimuth were essential for representing spatial patterns of slope attitude necessary for identifying dune slopes. Mean curvature provided important form-context to this determination. SADI was effective for characterizing dune boundaries, where differences in dune perimeter and height did not fully account for dune defects. Our object-oriented approach allowed us to adapt to natural scales of variation as represented by the size and shape of slope-facet units.

Key assumptions for the dune mapping process are based on the prototypical dune form and include: (1) only aeolian topography is represented in the DEMs; (2) only simple barchan or barchanoid dunes are being mapped; (3) the plain upon which dunes exist is nearly horizontal and featureless; (4) aeolian slopes are essentially tri-modal with steep lee slopes, moderate stoss slopes, and horizontal slopes; (5) an interdune area exists adjacent to or near most dunes; (6) dune altitude is statistically distinct from the interdune altitude; and (6) dune structure is broadly barchanoid and simple. These assumptions were reasonable for the study area and effective at partitioning dune-forms from the interdune area at White Sands National Park. Furthermore, although our approach was optimized for White Sands, we anticipate that our methods will perform well for dune fields that also reasonably conform to our key assumptions. Principal departures from our established assumptions are small areas of roads, man-made structures, and sparse vegetation.

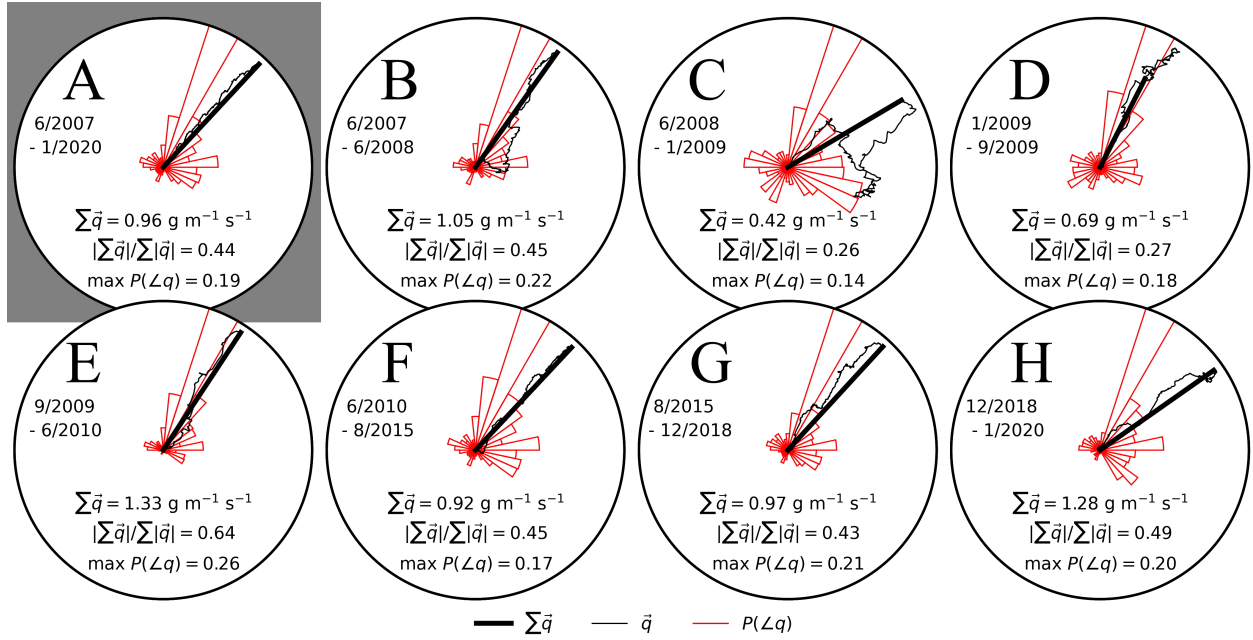


Figure 18: Potential sand flux estimated for (A) the entire observation period from 2007 through 2020, and for each time step: (B) June 2007 to June 2008, (C) June 2008 to January 2009, (D) January 2009 to September 2009, (E) September 2009 to June 2010, (F) June 2010 to August 2015, (G) August 2015 to December 2018, and (H) December 2018 to January 2020. The red rose shows the proportion of potential flux within a 12-degree azimuthal bin ($P(\angle q)$), which is overlain with cumulative flux vectors for each hourly measurement and net flux (\vec{q}). The magnitude of the resultant potential sand flux vector is indicated as $\sum \vec{q}$ and flux directionality as $|\sum \vec{q}| / \sum |\vec{q}|$. Flux is also presented in m² yr⁻¹ in Fig. 11 for comparison to measured dune characteristics and dynamics.

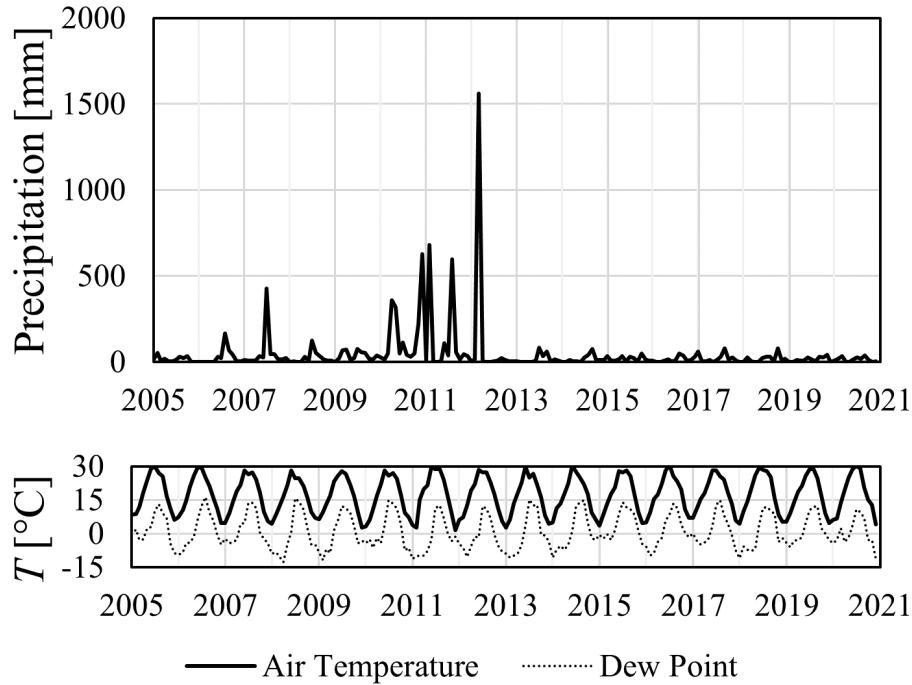


Figure 19: Sum monthly precipitation and mean temperature measured at the Holloman Air Force Base (KHMN).

Notable errors include the false inclusion of some roads (in the southern portion of the study area) and the rare omission of flat areas on the tops of some dunes. Mapping roads and other non-aeolian features as dunes can be resolved either by modeling these other features and specifically omitting them from analysis of aeolian morphologies, or by refining the model to more specifically define sand dunes. The omission errors of flat dune-tops relates to the evaluation of spatial scale and topographic context: the altitude variance in proximity to these locations was too great to conclude that slope-facet units located there were distinct from some substrate. Further research into assessing appropriate scale and semantic relationships in geomorphic systems, such as what "proximity" means and what is suitable as an interdune or "in-between" dune samples where dunes are tightly spaced, should resolve this issue.

We noted distinctive apparently artificial banding at the interface between certain subscenes (Figs. 14b, g, 15g, and 16g). The reason for the banding is two-fold. First, each quarter of the dune field is morphologically distinct as the dune field evolves from protodunes and dense longitudinal barchanoids in the western quarter to more sparse barchanoids in the west-central quarter, to dense longitudinal dunes in the east-central quarter, to parabolic dunes in the eastern quarter. Second, each processed section is empirically bound to the statistical distribution of slope angle and slope azimuth within that dataset for defining slope units and, ultimately, dune units, which is exacerbated by the morphological distinctness in each quarter. This had the most pronounced effect on inferred dune-unit orientation and on a time-step comparison for measuring migration rate and sand flux. Further research to substitute deterministic methods for empirical methods to derive distinct slope units is warranted for more spatially consistent results.

The process of modeling dunes within a structural framework exposed issues of boundaries, scale, and empiricism, including differentiating between classes of slope attitude, choosing the length-scale at which substrates are approximated, and choosing the scales at which curvature is relevant. The empirical classification method used to partition slope-facet units was particularly problematic, as it resulted in different dune-unit boundaries in overlapping areas, which challenged our ability to interpret lee slopes (e.g., Fig 14B,G) and measure structural changes over time. The size and shape of slope-units influence the altitude sampling when interpolating dune substrate surfaces, which impacts the dune-interdune classification.

Differently-sized and -shaped slope units will yield different dune-interdune boundaries and trade some low-amplitude features between the dune and interdune classes. In aggregate, these differences balance and are inconsequential in the statistical reduction of most dune-unit characteristics, where orientation-dependent characteristics appear to be most sensitive to differences in the resultant dune-unit boundaries (e.g., Fig. 14b, g). A deterministic method for defining elementary slope units will mitigate the resultant uncertainty, as will techniques for adaptively sampling a sufficiently large and diverse area for differentiating between relatively high and low altitude and for interpolating what is inferred to be the interdune plain as the dune substrate. One of our objectives was to formalize the concept of "sand dune" for mapping utilizing the topographic structure, but every component of a dune also requires formalization. A means for assessing the validity of each such formalization is also warranted for slope units and must extend beyond comparisons of area, perimeter, and other such geometric metrics, for what does it matter if a slope unit is larger, shorter, or rounder if it does not more fundamentally capture the elementary concept of "slope" in the fabric of the topography? Likewise, we presently have no means of measuring the dissonance between the concept and the formalization without resorting to another incompletely-defined model (e.g., manual mapping or a trained mapping AI), nor can we measure the magnitude of one's cognitive bias in the formulation of their mapping model compared to the *bona fide* landform, assuming the landform exists outside of our cognition of it (Deng, 2007). More research is needed on these complex topics in the context of geomorphological research.

More complex landforms with either require their own mapping models and/or a more expansive analysis of spatial hierarchical structure. For example, to map compound dunes, ripples on top of dunes, or interfering ripple patterns, there must be an accounting for the spatial containment and control imposed by the boundary conditions set by the larger entity. There currently exists no numerical framework for doing so and research is sorely needed in this area.

Computational scale is an as-yet unresolved issue in geomorphometry (Bishop et al., 2012, 2020). We must achieve a suitable level of generalization to map sand dunes and subdue small-scale bedforms. However, the desired scale varies spatially, and we do not have any clear theory or methods to determine a most-appropriate scale or set of scales given certain local or meso-scale conditions. Ridge units attempt to address this scale ambiguity, but a more fundamental analysis of scale is warranted. SADI falls short of its potential to map dune crestlines because of scale-variance in local divergence due to small-scale bedforms and blow-out features (e.g., Lee et al., 2019).

Our attempt to map crestlines according to cross-sectional maximum altitude yielded results inconsistent with what can be achieved with manual mapping. The mapped crestlines were visually smooth after several processing steps, but the culmination of that process translated mapped crestlines from their "true" locations at dune peaks and were commonly incomplete (Fig. 8). Other transect-based characterizations of crestlines that are effective where dune orientation is known and highly consistent (e.g., Cisneros et al., 2020) are not suitable where dune orientation is unknown or highly heterogeneous. "Crestline" is a semantic used to represent a low-frequency abstraction of the high-altitude portion of a dune, and is not well-represented as a line connecting altitude-maxima along the width of the dune. As crestlines are useful for characterizing dune structure, a more robust description of what they represent is warranted (e.g., Ewing et al., 2006; Rachal and Dugas, 2009; Ewing et al., 2015; Pedersen et al., 2015).

Because of the uncertainty associated with the empirical slope-unit classification and dune-unit partitioning, a statistical reduction of their measurable characteristics is a more reliable characterization of dune field morphology than any single dune unit's characterization. We found our statistical reductions to be comparable to the reductions or prior research. There is clearly a need for further research for more objective methods for greater spatial detail and temporal continuity in dune field characteristics, specifically to formalize dune-morphology semantics for mapping applications and to establish an operable framework for geomorphometric uncertainty characterization that does not depend on a subjective and surpassable benchmark for comparison (i.e., manual mapping).

6.2 Dune Field Characteristics

We compare our results with those of Baitis et al. (2014) because of their relatively extensive and comparable characterization of dune geometry. We note a significant difference in sample population from two perspectives: we measured an average of 2361 dunes that meet our filtering criteria in any given year (2038 if

excluding the 2018 and 2020 datasets, which have greater coverage) compared to their 171 dunes measured based on the June 2007 dataset. The boundaries mapped by Baitis et al. (2014) also differ from ours. The dunes measured by Baitis et al. (2014) are, on average, about three times the width of our dune units, and cover about three to four times the area. This is largely due to the aggressive dune-unit division used in our approach and their definition of a dune boundary which required contact with an interdune surface. Area 3 in Baitis et al. (2014) is most comparable to our zones b and c (Fig. 1), with 44 dunes in their study compared to about 130 dune units in any given year in our study. Area 4 in Baitis et al. (2014) is most comparable to our zone d, with 42 dunes in their study compared to about 80 dune units in any given year in our study.

We found dune height to be, on average, about 1 m shorter than those measured by Baitis et al. (2014). Though not explicitly stated, it appears that Baitis et al. (2014) measured dune height as the range between the minimum-altitude location along the dune's boundary to the maximum altitude on the dune's crest. We measured dune height as the difference between the land surface and a substrate interpolated from the adjacent interdune area, and we should expect this surface to almost always be higher than the lowest-altitude location on the dune unit boundary, resulting in a smaller height calculation.

Dune width and length average about 150 and 55 m, respectively. The dunes measured by Baitis et al. (2014) are about 450 m wide and 80 m long. The mean area and volume of our dunes (about 1000 m² and 30000 m³) is consequently also about a third of that measured by Baitis et al. (2014) (36140 m² and 123348 m³). This difference is due to the differences in mapping method, and highlights the tendency of our approach to aggressively divide dune units. This raises questions about what dune width means, or what defects constitute a dune boundary, particularly as White Sands contains very few isolated barchans to measure. Baitis et al. (2014) use a barchan-transverse dune to illustrate their methods with a barchan-transverse dune with no fewer than six horns, noses, or other convexities along its sinuous width. Many of our dune units exhibit two or fewer distinct convex or longitudinal features (Fig. 6A–D). This raises questions as to what constitutes a consistent selection for dune boundaries or for measuring dune width, volume, horn length, sinuosity, or any other parameter summarizing dune morphology. A continuous lee slope may serve as a contextual factor for unifying barchanoid shapes, though this is also sometimes problematic where dunes interact and a distinct steep (lee) slope may bridge two dune units across a thin mound of sand, or where the lee slope may climb onto the back of another dune.

We measure the mean orientation of the dune widthline to be about 350°, compared to the 338° measured by Baitis et al. (2014) and Ewing et al. (2006). We also measure a large population of dune units oriented about 100°, where aggressive unit division appears to have highlighted divisions between dominant dune orientations associated with barchan horns, spurs, convexities, and longitudinal defects. As with dune size, the difference is due to differences in dune boundaries, though dependencies on crestline and lee slope orientation are also implied in the method of Baitis et al. (2014). Overall, mean widthlines by the two methods are found to within 12° of each other, suggesting that the parameter is conceptually robust despite methodological differences to drawn dune boundaries or dune widthlines.

We found that any mapping of dune features to be highly dependent on spatial contextual information and knowledge of the functional relationships between geomorphological concepts. The concepts of dune width, length, crest, and interdune distance or length have historically been difficult to represent numerically and have resulted in a semantic vagueness in which experts intuitively grasp the same or similar concepts through use of such words as "crestline," "lee slope," or "dune wavelength" but without guarantee of precise replication (Fisher et al., 2005; Deng, 2007; Wernette et al., 2018a; Brierley et al., 2021; Young and Bishop, 2022). The method we used to map crestlines was insufficient because crestlines are not commonly crisp or obvious, and the definition for "crestline" was incongruous with our conceptual models and mapped features. Further research is needed to more robustly define geomorphological key concepts and processing for measuring dune field characteristics.

Our measured migration rates agree well with the average 3.6 m yr⁻¹ measured by Pedersen et al. (2015) between 2007 and 2010, with some segments that they monitored migrating in excess of 25 m in that time (Figs. 11, 15). McKee (1971) measured migration rates in excess of 10 m yr⁻¹ at the upwind edge of the dune field tapering to 1–3 m yr⁻¹ among the parabolic dunes in the east, with average migration rates of 1–4 m yr⁻¹ among the barchanoid dunes, which agrees well with our observations. The migration rate measured by Crabaugh (1994) of 1.4 m yr⁻¹ near the western edge of the dune field between June 1991 and October 1993 appears to have been a relatively slow migration period. Kocurek et al. (2007) inferred that sand dunes

at White Sands migrate at 1.5 m yr^{-1} based on observations of varves observed in an interdune area and assuming that 2/3 of the stratigraphy is missing, which agrees well with the measurements of Crabaugh (1994), although the alternative assumption that all stratigraphy is present yielded an estimate of 4.5 m yr^{-1} agrees more with our estimated mean of 3.65 m yr^{-1} .

Our flux estimates agree well with the estimates of Gunn et al. (2020) and Jerolmack et al. (2012), which predict peak sediment flux near the western edge at an average of $10\text{--}12 \text{ m}^2 \text{ s}^{-1}$ of the dune field that tapers eastward to $3\text{--}5 \text{ m}^2 \text{ s}^{-1}$ among the parabolic dunes from 2009–2010 (Figs. 11, 16). We further note relatively low sand flux in the central portion of the dune field before briefly increasing again just upwind of the parabolic dunes where flux again drops and reaches its lowest values (Fig. 16).

6.3 Dune Field Resilience

Developing automated methods for dune-field mapping provides a new approach to assess the resilience of dune fields to changes in boundary conditions induced by humans and climate change. Our assessment of key dune field parameters between 2007 and 2020 via automated mapping serves to assess changes in dune field morphology in the past 15 years, which we use to evaluate annual to decadal scale changes in the dunes and to assess the resilience of White Sands at these timescales. We have also generated baseline datasets of dune parameters and changes in dune parameters from which future data can be evaluated.

The concept of resilience is not well-formalized in geomorphology (Downes et al., 2013; Thoms et al., 2018), particularly given the complex interactions between sedimentary, hydrological, ecological, and climate systems, and the vast differences in timescales between observations, geomorphological change, and the rate at which changes occur in connected systems. Aeolian, fluvial, and coastal geomorphological change, however, occurs at spatial and temporal rates that are directly observable (e.g., Houser et al., 2015; Wernette et al., 2018b). We understand resilience within a tractable framework to reduce to these factors: (1) the magnitude of disturbances or stress that the system can absorb before manifesting change in measurable parameters from a nominal state (i.e., average or equilibrium); (2) the rate of change in measurable parameters; (3) the magnitude of disturbances or stress that the system can absorb before its nominal state changes; (4) the rate of change in the nominal state; and (5) the rate at which the system recovers or relaxes to its new or prior nominal state (Downes et al., 2013; Stallins and Corenblit, 2018). We therefore expect the White Sands Dune Field to manifest changes in dune characteristics or process rate magnitudes if it lacks resilience or is under the influence of some disturbance.

Recovery may follow cyclical patterns in complex hierarchies that organize time, space, and interdependent systems (i.e., "panarchies," Wohl, 2013; Wohl et al., 2014; Stallins and Corenblit, 2018). Resilience is inherently scale-dependent and coupled with other interdependent systems, being related to the magnitude, spatial distribution, and frequency of disturbances and systems responses (i.e., Houser et al., 2015; Wernette et al., 2018b). A dune field or other geomorphological system may effectively fully recover from an acute event, such as an intense storm, while drifting toward a new nominal state under chronic stresses, such as climate change and associated changes in regional wind regime, temperature, and precipitation. Our analysis of resilience is limited in three ways: (1) our data only accounts for eight observations over 13 years; (2) we focused our analysis only on the dune field topographic system; and (3) a nominal state for White Sands topography has yet to be defined, but may be characterized with the results of this study—the 2007 dataset serves as a benchmark for our comparisons. We therefore cannot describe White Sands resilience in the context of cyclical patterns and systems interactions, and further research and additional monitoring will be required to address resilience from a more holistic perspective.

Key variables relevant to dune field resilience that we monitored include dune migration rates, sand flux, and aggradation rates. Migration rate varied significantly, in excess of 5 m yr^{-1} in 2009–2010 and as slow as $2.07\text{--}2.64 \text{ m yr}^{-1}$ during slow years, with a mean of 3.65 m yr^{-1} from 2007–2020. Our slow-year estimates are faster than the long-term estimates of Kocurek et al. (2007) and Crabaugh (1994) at $1.4\text{--}1.6 \text{ m yr}^{-1}$ but within range of the measurements of McKee (1971) at $1.2\text{--}3.7 \text{ m yr}^{-1}$ for transverse and barchan dunes. McKee (1971) and Phillips et al. (2019) observed much more rapid migration rates among protodunes, which is corroborated with our observations (Fig. 15). Our sand flux estimates of $8.5 \text{ m}^2 \text{ yr}^{-1}$ (lowest $4.8 \text{ m}^2 \text{ yr}^{-1}$) also exceeded that predicted by Jerolmack et al. (2012) at $2.7 \text{ m}^2 \text{ yr}^{-1}$. Analyses of the LiDAR data show a net surface aggradation rate of 1.74 mm yr^{-1} from June 2007 to January 2020, which compares well with the OSL-based findings of Kocurek et al. (2007) ($1.2\text{--}1.7 \text{ mm yr}^{-1}$), and the predictions of Jerolmack et al.

(2012) (2.7 mm yr^{-1}), although the short-term accumulation inferred from cross-strata angle-of-climb by Kocurek et al. (2007) is significantly more rapid at 3.4 mm yr^{-1} . The migration rates that we observed from 2007 to 2020 are rapid relative to prior estimates of dune field averages, but within previously constrained ranges and otherwise consistent with predicted accumulation rates. Our results and comparisons with others' findings highlight White Sands' high degree of temporal variability and dependence on seasonal and annual wind and hydrological conditions (Newton and Allen, 2014; Newton and Land, 2016). These findings suggest that: (1) White Sands is susceptible to change with changes in the weather and climate; (2) White Sands dunes may have been migrating faster on average in the past two decades compared to its longer history; and (3) nominal behavior at White Sands encompasses a wide range of dynamic rates.

We interpret the variation between LiDAR datasets to be related to seasonal variations in response to variations in seasonal weather patterns. Although the year-on-year changes were small, seasonal variations measured between January 2009, September 2009, and June 2010 showed a marked shift in apparent sand volume between the spring and summer/fall (Table 8). We attribute this apparently extreme shift in sand volume to the September 2009 dataset having been captured following a series of easterly winds (Fig. 18D) that beveled dune lee slopes and redistributed sand to the interdune flats and stoss slope, resulting in an apparent degradation of the dune field, and were built back by the typical southwesterly winds (Fig. 18E), which dominate the spring season. Wind speed and variability appear to have a significant impact on sediment flux and associated dune migration rates. Transport rates were most rapid in 2009–2010 and 2018–2020, when winds were strong and focused compared to other years (Figs. 11I–J; 18). Our findings corroborate those of Pedersen et al. (2015), in that dune field morphology and transport is highly dependent upon its seasonal wind regime. Climate change that affects the strength, directionality, or seasonality of the regional wind regime will therefore likely result in different dune field behavior (see also Baas and Delobel, 2022).

The period of intense precipitation between 2010 and 2013 may have increased cohesion of dune surfaces and promoted the growth of stabilizing vegetation and consequently retarded dune migration rates between 2010 and 2018. Rachal and Dugas (2009) had noted a period of dune field reorganization associated with intense precipitation around 1985, particularly as an increase in the orderliness of dune structure manifest as an increase in crestline length and decrease in crestline sinuosity and density of crestline terminations. Although we were unable to reliably extract dune crestlines, we may interpret the number of dune units as proportional to the number of crestline terminations, assuming that dune-unit boundaries represent dune defects and that crestlines would therefore tend to terminate at or prior to dune-unit boundaries. We observe a subtle tendency toward fewer dune units in zones b, c, d, and e over time (Table 6) and toward larger and less-compact (longer) dune units over time (Figs. 11B–E, G). We interpret these signals as indications that dunes tended toward greater orderliness on the decade-scale from 2007 to 2020, paralleling the interpretation that fewer defects correspond to more ordered, mature dunes (e.g., Werner and Kocurek, 1999; Ewing and Kocurek, 2010). This pattern is typical and expected as dunes mature across the dune field, but our analysis considers the aggregate of the entire dune field, suggesting: (1) the dune field is not at a state of equilibrium where new dunes are created at the same rate as old dunes merge within the observed time period; (2) the dune field overall is maturing; and/or (3) a shift in boundary conditions favors greater orderliness. Our observed trend toward orderliness conflicts with the conclusion of Rachal and Dugas (2009) that finds a decrease in orderliness on a larger timescale with fewer observations (5 images over 55 years compared to our 8 DEMs over 13 years) and which identified dune crestlines using imagery rather than dune three-dimensional structure. We expect more significant changes in dune field structure to manifest at larger timescales, when dunes have migrated at least half their wavelength (McElroy and Mohrig, 2009), or at least 33 years, given our average migration rate of 3.56 m yr^{-1} . We may have captured a shorter-timescale phenomenon suggested by Rachal and Dugas (2009), however, where they speculated that wet years may lead to a period of relaxation and organization, which the 2010–2013 precipitation may account for. We also found seasonality to be important in assessing changes in dune morphology, and we do not have good control on when the images used by Rachal and Dugas (2009) were captured.

A key factor not studied here, but has the significant ability to impact the dune morphology and dynamics as measured in this study is the water table at White Sands. It plays an important role in the stability of the system by increasing cohesion of the interdune and dune surfaces and the resistance of these surfaces to erosion (Newton and Allen, 2014; Newton and Land, 2016). Increased population and demand for water in the Tularosa Basin has resulted in an increase in water withdraw from basin water reservoirs (Huff,

2005; Newton and Land, 2016). Within the dune field, two aquifers exist that affect the production of sand and stabilization of the dune field. Groundwater tapped from the deeper aquifer provides some regional recharge to the shallow aquifer beneath the dune field, and supplies water to the lower-elevation playas that generate the modern sand supply for the dune field (Newton and Allen, 2014). A shallow perched aquifer sits at the surface within the dune field that accumulates below the active dunes and stabilizes the dunes by cohesion of the gypsum sand. Increased water use or changes in climate variables including temperature, precipitation, and windiness could affect these reservoirs, which could in turn affect supply to the dune field or stability of the dune field. These changes could also affect an increase or decrease in the amount and coverage of vegetation across the dune field. Basin-wide ground water monitoring has been implemented in the past few years, but a long enough baseline does not yet exist to make a robust comparison to the dune morphodynamics. We did not attempt to relate changes in dune field topography to changes in the water table, but ongoing monitoring of both the topography and water table could provide a strong assessment of resilience.

Continued observations will be required to confirm and give greater context to the trends that we observed. Dune morphology decorrelates when dunes have traveled about half of their wavelength, indicating novel dune morphologies (McElroy and Mohrig, 2009). We therefore recommend continued monitoring for at least two of these decorrelation cycles, or one full wavelength. Given the average migration rate of 3.65 m yr^{-1} and a typical wavelength of about 200 m, dunes will have migrated a full wavelength by 2062 (55 years from 2007). Tracking dunes across time for analyses of changes in individual dune morphology and structure will be most reliably achieved with considerable spatial overlap between dunes at different time steps, so surveys should be repeated before dunes migration half their length. Assuming Gaussian distributions, 95% of dunes have a length of at least 33.67 m and migrate up to 11.83 m yr^{-1} , suggesting that surveys should be repeated at least every two years. Alternatively, a less frequent survey could occur once every five years to accommodate the average dune length 54.67 m and average migration rate on a fast year of 4.57 m yr^{-1} . With frequent (annual or bi-annual) monitoring, it may also be possible to observe system response to acute disturbances, such as the 2012 precipitation event that we could not observe in the morphology due to a 5-year monitoring hiatus. We strongly recommend that future surveys record dune field topography in the same season, preferably the early summer after the main flux season but before significant bevelling due to summer and autumn winds (i.e., June; Fig. 17).

7 Conclusions

We have presented an application of a topographic structural framework for representing geomorphological concepts (Lastochkin et al., 2018; Young and Bishop, 2022) in the context of aeolian geomorphological research. We found a formalization of the spatial hierarchical structure of dune field topography to be effective for differentiating between dunes and the interdune and for formalizing spatial concepts related to dune geomorphology. This analysis made characterization of the entire dune field feasible, highlighting patterns in dune morphology in relation to dune defects and apparent vegetation patterns. We found that the dune field has no distinct morphological response to extreme weather events, but identified a subtle trend toward dune orderliness (fewer, larger dune units). Our results also suggest that dune migration and sand flux are dependent on strong, seasonal southwesterly winds and may be influenced by high-magnitude precipitation events. These factors were conflated during the study period, but wind strength and directionality appears to have a stronger impact on dune field dynamics than precipitation. Continued biannual to semi-decadal monitoring of dune field topography will be important for identifying long-term trends and placing our observations into greater context.

The process of employing a spatial hierarchical framework for analyzing the topography also highlighted important incongruities between our conceptual models and the feature definitions provided in the literature, which provides research opportunities for representing numerous geomorphological concepts with semantic models. Vagueness may be unavoidable in many cases, because geomorphic objects commonly have indistinct or context-sensitive boundaries (Fisher et al., 2005; Deng, 2007; Wernette et al., 2018a). Though recent methods have found success in utilizing machine learning techniques to extract dunes (e.g., Rubanenko et al., 2021), how a dune is defined and drawn influences its measurement (Wernette et al., 2018a), and it therefore behooves geomorphologists to be clear when communicating dunes and other geomorphic features

and to seek to provide and use a replicable model for knowledge-based mapping. Despite the semantic vagueness associated with sand dunes and their constituent features (e.g., crestlines), difficulty with certain morphometric parameters (i.e., interdune distance), and the biases built into manual mapping techniques, our assessment of key dune parameters agreed well with manual maps. The filtering we applied to our dunes was motivated by known computational issues, such as substrate predictions and single-pixel dune units, rather than an attempt to ignore "less ideal" dunes. We believe that multiple levels of land-surface abstraction are important for addressing issues of scale and for future deterministic and probabilistic mapping approaches that are less reliant on empirical (non-physical) parameters and training, reduce sampling bias, increase replicability, and promote clarity and interoperability through the development and sharing of semantic models that the scientific community can dissect, test, and improve.

Our approach to land-surface characterization bears obvious applications to planetary and exploration research. Numerous landforms and process-form relationships require more robust definition, however, to achieve accurate automated mapping and interpretation of the surface of the Earth and extraplanetary bodies, particularly in relation to hazards, landing-site suitability, science-priority identification, habitability, and the search for life. The integration of optical, thermal, and other spatial or spectral data will provide additional context to assist in these efforts.

Data Availability

Data and code necessary to replicate this research can be found in the Texas Data Repository, DOI: 10.18738/T8/1KW6W2. <https://dataverse.tdl.org/dataset.xhtml?persistentId=doi:10.18738/T8/1KW6W2>

Acknowledgments

We thank the Jackson School of Geosciences at the University of Texas at Austin, U.S. Geological Survey, U.S. National Park Service, NSF NCALM Seed Grant, White Sands National Park, and OpenTopography.org for acquiring data and making the data available. We thank Andrew Gunn for providing assistance in modeling sand flux. This work was supported in part by the National Park Service through Task Agreement P18AC00855 and NASA grant #80NSSC17K0763 to RCE. We thank our anonymous reviewers for their care and attention.

References

- Ahmedou, D. O., Mahfoudh, A. O., Dupont, P., El Moctar, A. O., Valance, A., and Rasmussen, K. R. (2007). Barchan dune mobility in mauritania related to dune and interdune sand fluxes. *Journal of Geophysical Research*, 112:F02016.
- Allen, B., Love, D., and Myers, R. (2009). Evidence for late pleistocene hydrologic and climatic change from lake otero, tularosa basin, south-central new mexico. *New Mexico Geology*, 31(1):9–25.
- Alvioli, M., Guzzetti, F., and Marchesini, I. (2020). Parameter-free delineation of slope units and terrain subdivision of italy. *Geomorphology*, 358:107124.
- Anders, K., Winiwarter, L., Lindenbergh, R., Williams, J. G., Vos, S. E., and Höfle, B. (2020). 4d objects-by-change, spatiotemporal segmentation of geomorphic surface change from lidar time series. *ISPRS Journal of Photogrammetry and Remote Sensing*, 159:352–363.
- Baas, A. C. W. and Delobel, L. A. (2022). Desert dunes transformed by end-of-century changes in wind climate. *Nature Climate Change*, 12:999–1006.
- Bagnold, R. (1941). *The Physics of Wind-Blown Sand and Desert Dunes*. Methuen, London.
- Baitis, E., Kocurek, G., Smith, V., Mohrig, D., Ewing, R. C., and Peyret, A.-P. (2014). Definition and origin of the dune-field pattern at white sands, new mexico. *Aeolian Research*, 15:269–287.

- Bishop, M. P. and Houser, C. (2016). Geomorphological mapping and geospatial technology. *International Encyclopedia of Geography: People, the Earth, Environment and Technology*, pages 1–13.
- Bishop, M. P., James, L. A., Shroder, Jr., J. F., and Walsh, S. J. (2012). Geospatial technologies and digital geomorphological mapping: Concepts, issues and research. *Geomorphology*, 137:5–26.
- Bishop, M. P., Young, B. W., Huo, D., and Chi, Z. (2020). Spatial analysis and modeling in geomorphology. In *Reference Module in Earth Systems and Environmental Sciences*. Elsevier.
- Bond, C. E. (2015). Uncertainty in structural interpretation: Lessons to be learnt. *Journal of Structural Geology*, 75:185–200.
- Bond, C. E., Gibbs, A. D., Shipton, Z. K., and Jones, S. (2007). What do you think this is? ”conceptual uncertainty” in geoscience interpretation. *GSA Today*, 17(11):4–10.
- Breed, C. S. and Grow, T. A. (1979). Morphology and distribution of dunes in sand seas observed by remote sensing. In *A Study of Global Sand Seas*, volume 1052 of *Professional Paper*, pages 253–302. United States Geological Survey.
- Brierley, G., Fryirs, K., Reid, H., and Williams, R. (2021). The dark art of interpretation in geomorphology. *Geomorphology*, 390:107870.
- Burrough, P. A. and Frank, A. U. (1996). *Geographic objects with indeterminate boundaries*, volume 2 of *GISDATA*. Taylor & Francis, Bristol, PA, USA.
- Cisneros, J., Best, J., van Dijk, T., de Almeida, R. P., Amsler, M., Boldt, J., Freitas, B., Galeazzi, C., Huizinga, R., Ianniruberto, M., Ma, H., Nittrouer, J. A., Oberg, K., Orfeo, O., Parsons, D., Szupiany, R., Wang, P., and Zhang, Y. (2020). Dunes in the world’s big rivers are characterized by low-angle lee-side slopes and a complex shape. *Nature Geoscience*, 13:156–162.
- Claudin, P. and Andreotti, B. (2006). A scaling law for aeolian dunes on mars, venus, earth, and for subaqueous ripples. *Earth and Planetary Science Letters*, 252(1–2):30–44.
- Crabaugh, M. M. C. (1994). *Controls on Accumulation in Modern and Ancient Wet Eolian Systems*. PhD thesis, The University of Texas at Austin, Austin, TX, USA.
- Dao, D. V., Jaafari, A., Bayat, M., Mafi-Gholami, D., Qi, C., Moayedi, H., Phong, T. V., Ly, H.-B., Le, T.-T., Trinh, P. T., Luu, C., Quoc, N. K., Thanh, B. N., and Pham, B. T. (2020). A spatially explicit deep learning neural network model for the prediction of landslide susceptibility. *Catena*, 188:104451.
- Davis, J. M., Grindrod, P. M., Boazman, S. J., Vermeesch, P., and Baird, T. (2020). Quantified aeolian dune changes on mars derived from repeat context camera images. *Earth and Space Science*, 7:e2019EA000874.
- Day, M. and Kocurek, G. (2018). Pattern similarity across planetary dune fields. *Geology*, 46(11):999–1002.
- Deng, Y. (2007). New trends in digital terrain analysis: landform definition, representation, and classification. *Progress in Physical Geography*, 31(4):405–419.
- Downes, B. J., Miller, F., Barnett, J., Glaister, A., and Ellemor, H. (2013). How do we know about resilience? an analysis of empirical research on resilience, and implications for interdisciplinary praxis. *Environmental Research Letters*, 8(1):014041.
- Dramis, F., Guida, D., and Cestari, A. (2011). Chapter three - nature and aims of geomorphological mapping. In Smith, M. J., Paron, P., and Griffiths, J. S., editors, *Geomorphological Mapping*, volume 15 of *Developments in Earth Surface Processes*, pages 39–73. Elsevier.
- Duran Vincent, O., Andreotti, B., Claudin, P., and Winter, C. (2019). A unified model of ripples and dunes in water and planetary environments. *Nature Geoscience*, 12(5):345–350.

- Eastwood, E. N., Kocurek, G., Mohrig, D., and Swanson, T. (2012). Methodology for reconstructing wind direction, wind speed and duration of wind events from aeolian cross-strata. *Journal of Geophysical Research*, 117:F03035.
- Eisank, C. (2010). A hierarchical system for multi-scale and object-based landform classification. In Wallgrün, J. O. and Lautenschütz, A.-K., editors, *Proceedings of the GIScience 2010 Doctoral Colloquium*, pages 17–22, Zurich, Switzerland.
- Eisank, C., Drăguț, L., and Blaschke, T. (2011). A generic procedure for semantics-oriented landform classification using object-based image analysis. In *Proceedings of Geomorphometry 2011*, pages 125–128, Redlands, California, USA.
- Emran, A., Marzen, L. J., and King Jr., D. T. (2020). Semiautomated identification and characterization of dunes at hargraves crater, mars. *Earth and Space Science*, 7:e2019EA00093.
- Ewing, R. (2012). White Sands National Monument, NM: Lidar survey of dune fields (june 2010). data accessible at <https://doi.org/10.5069/G97D2S2D>.
- Ewing, R. C. (2020). White sands. In Lancaster, N. and Hesp, P., editors, *Inland Dunes of North America. Dunes of the World.*, pages 207–237. Springer, Cham, Switzerland.
- Ewing, R. C. and Kocurek, G. (2010). Aeolian dune-field pattern boundary conditions. *Geomorphology*, 114:175–187.
- Ewing, R. C., McDonald, G. D., and Hayes, A. G. (2015). Multi-spatial analysis of aeolian dune-field patterns. *Geomorphology*, 240:44–53.
- Ewing, R. C. E., Kocurek, G., and Lake, L. W. (2006). Pattern analysis of dune-field parameters. *Earth Surface Processes and Landforms*, 31:1176–1191.
- Fisher, P., Wood, J., and Cheng, T. (2005). Fuzziness and ambiguity in multi-scale analysis of landscape morphometry. In Petry, F. E., Robinson, V. B., and Cobb, M. A., editors, *Fuzzy Modeling with Spatial Information for Geographic Problems*, pages 209–232. Springer.
- Fryberger, S. G. and Dean, G. (1979). Dune forms and wind regime. In McKee, E. D., editor, *A Study of Global Sand Seas*, number 1052 in U.S. Geological Survey Professional Paper, pages 137–169. U.S. Government Printing Office, Washington, D.C., USA.
- Gadal, C., Narteau, C., Ewing, R. C., Gunn, A., Jerolmack, D., Andreotti, B., and Claudin, P. (2020). Spatial and temporal development of incipient dunes. *Geophysical Research Letters*, 47:e2020GL088919.
- Gaurav, S. and Mark, D. (2010). Cognition based extraction and modeling of topographic eminences. *Cartographica*, 45(2):105–112.
- Grohmann, C. H., Garcia, G. P. B., Affonso, A. A., and Albuquerque, R. W. (2020). Dune migration and volume change from airborne lidar, terrestrial lidar and structure from motion-multi view stereo. *Computers and Geosciences*, 143:104569.
- Gunn, A., Casasanta, G., Di Liberto, L., Falcini, F., Lancaster, N., and Jerolmack, D. J. (2022a). What sets aeolian dune height? *Nature Communications*, 13:2401.
- Gunn, A., Rubanenko, L., and Lapôtre, G. A. (2022b). Accumulation of windblown sand in impact craters on mars. *Geology*, XX(X):5.
- Gunn, A., Schmutz, P., Wanker, M., Edmonds, D. A., Ewing, R. C., and Jerolmack, D. J. (2020). Macroscopic flow disequilibrium over aeolian dune fields. *Geophysical Research Letters*, 47:e2020GL088773.
- Heckmann, T., Schwanghart, W., and Philips, J. D. (2015). Graph theory—recent developments of its application in geomorphology. *Geomorphology*, 243:130–146.

- Hoeser, T. and Kuenzer, C. (2020). Object detection and image segmentation with deep learning on earth observation data: A review-part i: Evolution and recent trends. *Remote Sensing*, 12:1667.
- Houser, C., Wernette, P., Rentschlar, E., Jones, H., Hammond, B., and Trimble, S. (2015). Post-storm beach and dune recovery: Implications for barrier island resilience. *Geomorphology*, 234:54–63.
- Huff, G. F. (2005). Simulation of ground-water flow in the basin-fill aquifer of the tularosa basin, south-central new mexico, predevelopment through 2040. Scientific Investigations Report 2004–5197, U.S. Geological Survey, Reston, Virginia.
- Jenness, J. S. (2004). Calculating landscape surface area from digital elevation models. *Wildlife Society Bulletin*, 32(3):829–839.
- Jerolmack, D. J., Ewing, R. C., Falcini, F., Martin, R. L., Masteller, C., Phillips, C., Reitz, M. D., and Buynevich, I. (2012). Internal boundary layer model for the evolution of desert dune fields. *Nature Geoscience*, 5(3):206–209.
- Jerolmack, D. J., Reitz, M. D., and Martin, R. L. (2011). Sorting out abrasion in a gypsum dune field. *Journal of Geophysical Research*, 116:F02003.
- Kocurek, G. (2013a). White Sands National Monument, NM: Lidar survey of dune fields (jan 2009). data accessible at <https://doi.org/10.5069/G9Q23X5P>.
- Kocurek, G. (2013b). White Sands National Monument, NM: Lidar survey of dune fields (sept 2009). data accessible at <https://doi.org/10.5069/G9ZK5DMD>.
- Kocurek, G., Carr, M., Ewing, Havholm, K. G., Nagar, Y. C., and Singhbi, A. K. (2007). White sands dune field, new mexico: Age, dune dynamics and recent accumulations. *Sedimentary Geology*, 197(3):313–331.
- Kocurek, G. and Ewing, R. (2020a). 2007 White Sands Dune Field LiDAR topographic data. data accessible at <https://doi.org/10.18738/T8/WUNF0G>.
- Kocurek, G. and Ewing, R. (2020b). 2008 White Sands Dune Field LiDAR topographic data. data accessible at <https://doi.org/10.18738/T8/HQVUSX>.
- Kocurek, G. and Ewing, R. C. (2016). Trickle-down and trickle-up boundary conditions in eolian dune-field pattern formation. In Budd, D. A., Hajek, E. A., and Purkis, S. J., editors, *Autogenic Dynamics and Self-Organization in Sedimentary Systems*, volume 106. SEPM Society for Sedimentary Geology.
- Lancaster, N. (1995). Origin of the gran desierto sand sea, sonora, mexico: Evidence from dune morphology and sedimentology. In Tchakerian, V. P., editor, *Desert Aeolian Processes*, pages 11–35. Chapman & Hall, London, UK.
- Langford, R. P. (2003). The holocene history of the white sands dune field and influences on eolian deflation and playa lakes. *Quaternary International*, 104(1):31–39.
- Lastochkin, A. N., Zhirov, A. I., and Boltramovich, S. F. (2018). System-morphological approach: Another look at morphology research and geomorphological mapping. *Geomorphology*, 303:486–503.
- Lee, D. B., Ferdowsi, B., and Jerolmack, D. J. (2019). The imprint of vegetation on desert dune dynamics. *Geophysical Research Letters*, 46(21):12041–12048.
- MacMillan, R. A. and Shary, P. A. (2009). Landforms and landform elements in geomorphometry. In Hengl, T. and Reuter, H. I., editors, *Geomorphometry: Concepts, software, applications*, volume 33 of *Developments in Soil Science*, pages 227–254. Elsevier, New York, NY, USA.
- Martin, R. L. and Kok, J. F. (2017). Wind-invariant saltation heights imply linear scaling of aeolian saltation flux with shear stress. *Science Advances*, 3(6):e1602569.
- McElroy, B. and Mohrig, D. (2009). Nature of deformation of sandy bed forms. *Journal of Geophysical Research*, 114:F00A04.

- McKee, E. D. (1966). Structures of dunes at white sands national monument, new mexico (and a comparison with structures of dunes from other selected areas). *Sedimentology*, 7(1):3–69.
- McKee, Edwin D. and Douglass, J. R. (1971). Growth and movement of dunes at white sands national monument, new mexico. Professional Paper 750-D, United States Geological Survey, Washington, D.C., USA.
- Minár, J. and Evans, I. S. (2008). Elementary forms for land surface segmentation: The theoretical basis of terrain analysis and geomorphological mapping. *Geomorphology*, 95:236–259.
- Minár, J., Evans, I. S., and Jenčo, M. (2020). A comprehensive system of definitions of land surface (topographic) curvatures, with implications for their application in geoscience modelling and prediction. *Earth-Science Reviews*, 211:103414.
- Newton, B. T. and Allen, B. (2014). Hydrologic investigation at white sands national monument. Open-File Report 559, New Mexico Bureau of Geology and Mineral Resources, Socorro, NM, USA.
- Newton, B. T. and Land, L. (2016). Brackish water assessment in the eastern tularosa basin, new mexico. Open-file Report 582, New Mexico Bureau of Geology and Mineral Resources, Socorro, NM, USA.
- Olaya, V. (2009). Basic land-surface parameters. In Hengl, T. and Reuter, H. I., editors, *Geomorphometry: Concepts, software, applications*, volume 33 of *Developments in Soil Science*, pages 141–169. Elsevier, New York, NY, USA.
- Pedersen, A., Kocurek, G., Mohrig, D., and Smith, V. (2015). Dune deformation in a multi-directional wind regime: White sands dune field, new mexico. *Earth Surface Processes and Landforms*, 40:925–941.
- Pelletier, J. D. and Jerolmack, D. J. (2014). Multiscale bed form interactions and their implications for the abruptness and stability of the downwind dune field margin at white sands. *Journal of Geophysical Research: Earth Science*, 119:2396—2411.
- Phillips, J. D., Ewing, R. C., Bowling, R., Weymer, B. A., Barrineau, P., and Nittrouer, J. A. (2019). Low-angle eolian deposits formed by protodune migration, and insights into slipface development at white sands dune field, new mexico. *Aeolian Research*, 36:9–26.
- Rachal, D. M. and Dugas, D. P. (2009). Historical dune pattern dynamics: White sands dune field, new mexico. *Physical Geography*, 30(1):64–78.
- Reitz, M. D., Jerolmack, D. J., Ewing, R. C., and Martin, R. L. (2010). Barchan-parabolic dune pattern transition from vegetation stability threshold. *Geophysical Research Letters*, 37:L19402.
- Rubanenko, L., Pérez-López, S., Schull, J., and Lapôtre, M. G. A. (2021). Automatic detection and segmentation of barchan dunes on mars and earth using a convolutional neural network. *IEEE Journal of Selected Topics in Applied Earth Observations and Remote Sensing*, 14:9364–9371.
- Shary, P. A., Sharaya, L. S., and Mitusov, A. V. (2002). Fundamental quantitative methods of land surface analysis. *Geoderma*, 107:1–32.
- Stallins, J. A. and Corenblit, D. (2018). Interdependence of geomorphic and ecologic resilience properties in a geographic context. *Geomorphology*, 305:76–93.
- Swanson, T., Mohrig, D., and Kocurek, G. (2016). Aeolian dune sediment flux variability over an annual cycle of wind. *Sedimentology*, 63:1753–1764.
- Szynkiewicz, A., Ewing, R. C., Moore, C. H., Glamoclija, M., Bustos, D., and Pratt, L. M. (2010). Origin of terrestrial gypsum dunes—implications for martian gypsum-rich dunes of olympia undae. *Geomorphology*, 121(1–2):69–83.
- Thoms, M. C., Piégay, H., and Parsons, M. (2018). What do you mean, ‘resilient geomorphic systems’? *Geomorphology*, 305:8–19.

- Thorsnes, T., Bjarnadóttir, L. R., Jarna, A., Baeten, N., Scott, G., Guinan, J., Monteys, X., Dove, D., Green, S., Gafeira, J., and Stevenson, A. (2018). National programmes: Geomorphological mapping at multiple scales for multiple purposes. In Micallef, A., Krastel, S., and Savini, A., editors, *Submarine Geomorphology*, pages 535–552. Springer International Publishing, Cham.
- USGS (2017). USGS LPC NM WhiteSands 2015 LAS 2017. data accessible at https://portal.opentopography.org/usgsDataset?dsid=USGS_LPC_NM_WhiteSands_2015_LAS_2017.
- USGS (2020). NM SouthEast B4 2018. data accessible at https://portal.opentopography.org/usgsDataset?dsid=NM_SouthEast_B4_2018.
- USGS (2021). NM WhiteSandsNM 2020. data accessible at https://portal.opentopography.org/usgsDataset?dsid=NM_WhiteSandsNM_2020.
- Vaz, D. A., Sarmiento, P. T. K., Barata, M. T., Fenton, L. K., and Michaels, T. I. (2015). Object-based dune analysis: Automated dune mapping and pattern characterization for ganges chasma and gale crater, mars. *Geomorphology*, 250:128–139.
- Vermeesch, P. and Drake, N. (2008). Remotely sensed dune celerity and sand flux measurements of the world’s fastest barchans (Bodélé, Chad). *Geophysical Research Letters*, 35(24):L24404.
- Watkins, J. S., Walters, L. A., and Godson, R. H. (1972). Dependence of in-situ compressional-wave velocity on porosity in unsaturated rocks. *Geophysics*, 37(1):29–35.
- Werner, B. T. (1999). Complexity in natural landform patterns. *Science*, 284(5411):102–104.
- Werner, B. T. and Kocurek, G. (1999). Bedform spacing from defect dynamics. *Geology*, 27(8):727–730.
- Wernette, P., Thompson, S., Eyler, R., Taylor, H., Taube, C., Medlin, A., Decuir, C., and Houser, C. (2018a). Defining dunes: Evaluating how dune feature definitions affect dune interpretations from remote sensing. *Journal of Coastal Research*, 34(6):1460–1470.
- Wernette, P. A., Houser, C., Weymer, B. A., Everett, M. E., Bishop, M. P., and Reece, B. (2018b). Directional dependency and coastal framework geology: implications for barrier island resilience. *Earth Surface Dynamics*, 6(4):1139–1153.
- Wheaton, Joseph M. Fryirs, K. A., Brierley, G., Bangen, S. G., Bouwes, N., and O’Brien, G. (2015). Geomorphic mapping and taxonomy of fluvial landforms. *Geomorphology*, 248:273–295.
- Wilson, J. S. J., Chandrasekar, N., and Magesh, N. S. (2012). Morphometric analysis of major sub-watersheds in aiyar and karai pottanar basin, central tamil nadu, india using remote sensing and gis techniques. *Bonfring International Journal of Industrial Engineering and Management Science*, 2(1):8–15.
- Wohl, E. (2013). The complexity of the real world in the context of the field tradition in geomorphology. *Geomorphology*, 200:50–58.
- Wohl, E., Gerlak, A. K., Poff, N. L., and Chin, A. (2014). Common core themes in geomorphic, ecological, and social systems. *Environmental Management*, 53:14–27.
- Wood, J. (1996). Scale-based characterisation of digital elevation models. In Parker, D., editor, *Innovations in GIS 3*, pages 163–176. Taylor and Francis, London, UK.
- Xie, Z., Haritashya, U. K., Asari, V. K., Young, B. W., Bishop, M. P., and Kargel, J. S. (2020). Glaciernet: A deep-learning approach for debris-covered glacier mapping. *IEEE Access*, 8.
- Young, B. W. and Bishop, M. P. (2022). Mountain process regime characterization using a topographic morphological structural framework. *Physical Geography*, 0(0):1–37.
- Zhang, X., Xiao, P., and Feng, X. (2020). Object-specific optimization of hierarchical multiscale segmentations for high-spatial resolution remote sensing images. *ISPRS Journal of Photogrammetry and Remote Sensing*, 159:308–321.